

Mathias Harper

The Digital Wheelchair Project: Motion Tracking, Mathematical Modeling and Identification.

Master's thesis in Cybernetics and Robotics
January 2022

Mathias Harper

The Digital Wheelchair Project: Motion Tracking, Mathematical Modeling and Identification.

Master's thesis in Cybernetics and Robotics
January 2022

Norwegian University of Science and Technology

The Digital Wheelchair Project: Motion Tracking, Mathematical Modeling and Identification.

Mathias Furseth Harper

July 4, 2022

Preface

This thesis was written in the final semester of the Master's programme in Cybernetics and Robotics at the Norwegian University of Science and Technology (NTNU) in Trondheim. It constitutes the completion of my studies at the Department of Engineering Cybernetics within the field of Biomedical Cybernetics.

My interest in dynamical systems and biomedical cybernetics motivated me to work on this topic. Working with a problem with such important real-life applications was very inspiring. The potential of helping wheelchair users lead more healthy lifestyles has been a true motivation for completing this thesis.

I would like to thank my supervisors, Damiano Varagnolo and Roya Doshmanziari, for their very helpful guidance and insight. A big thanks to Damiano for formulating the project and entrusting me with it. I would especially like to thank Roya for her thorough help during the research and writing phases of the project.

Finally, i would like to thank my family for their continuing support.

Abstract

Many wheelchair users lead physically inactive lifestyles due to limited movement options and overall disabilities. This lack of physical activity may seriously affect their physical and mental conditions. In this thesis, we investigate the possibilities of estimating the energy expenditure and physical activity in wheelchair users using their motion-captured trajectories during exercise.

Two models were derived with the intent to parameterize the movement of the participants in the study, a model based on the double pendulum and a model based on the Van der pol oscillator. The parameters were later determined using least squares estimation and derivative-free optimization in order to analyze their correlation to energy expenditure, heart rate, and other demographic variables.

The results show that the double pendulum model performs poorly, and its estimated parameters show no correlation to energy expenditure or heart rate. On the other hand, the van der pol model shows some promise, as, under specific circumstances, correlations between energy expenditure and heart rate were observed.

Sammendrag

Mange rullestolbrukere lever en fysisk inaktiv livsstil på grunn av begrensede bevegelsesmuligheter og generelle funksjonshemninger. Denne mangelen på fysisk aktivitet kan ha alvorlige implikasjoner på både deres fysiske og mentale helse. I denne oppgaven undersøker vi mulighetene for å estimere energiforbruket og hjerterefrekvensen hos rullestolbrukere ved å bruke bevegelsesbanene til armene deres under trening.

To modeller ble utledet med hensikten å parameterisere bevegelsen til deltakerne i studiet, en modell basert på det doble pendelet og en modell basert på Van der pol-oscillatoren. Parametrene ble så regnet ut ved bruk av minste kvadraters estimering og derivatfri optimalisering. Videre ble de estimerte parametrenes korrelasjon til energiforbruk, hjerterefrekvens og andre demografiske variabler undersøkt.

Resultatene viser at den doble pendelmodellen yter dårlig, og dens estimerte parametere viser ingen korrelasjon til energiforbruk eller hjerterefrekvens. Van der pol-modellen viser mer lovende resultater, siden det under spesifikke omstendigheter ble observert korrelasjoner mellom de estimerte parametrene og energiforbruk og hjerterefrekvens.

Contents

Preface	i
Abstract	ii
Sammendrag	iii
Contents	iv
Figures	vi
Tables	ix
1 Introduction	1
1.1 Motivation and Background	1
1.2 The cross-sectional study	1
1.2.1 Participants	2
1.2.2 Test protocol	2
1.2.3 Equipment	3
1.3 Scope and Research Objectives	3
2 Theory	4
2.1 The Van der Pol unforced oscillator	4
2.1.1 The limit cycle of the Van der Pol oscillator	5
2.1.2 Power expansion	6
2.2 Mathematical modelling of the double pendulum	7
2.2.1 Lagrangian mechanics	7
2.2.2 External forces in Lagrangian mechanics	8
2.2.3 The dynamics of the double pendulum	9
2.3 Numerical methods for solving ODEs	12
2.3.1 Runge-Kutta 4	12
2.3.2 Adams–Moulton methods	13
2.4 Least squares estimation	13
2.5 Measurements of performance	13
2.5.1 Mean Square Error	14
2.5.2 Root Mean Square Error	14
2.5.3 FIT	14
2.6 Principal Component Analysis	14
2.6.1 Singular Value Decomposition	14
2.6.2 Derivation of PCA through singular value decomposition	15
2.6.3 Dimensionality Reduction	15
3 Method and set-up	16
3.1 Motion trajectories	16

3.2	Energy expenditure	17
3.3	Preprocessing of the data	18
3.3.1	Preprocessing for the double pendulum estimator	18
3.3.2	Preprocessing for the Van Der Pol estimator	21
3.4	Energy expenditure and heart rate centroids	22
3.5	Modeling of external forces and damping	23
3.6	Estimating F_1 and F_2	25
3.6.1	Parameter selection	26
3.6.2	Constraint selection	27
3.7	The Van der Pol estimator	27
3.7.1	Selection of approximation order	27
3.7.2	Deriving the estimator	30
4	Results	32
4.1	Double Pendulum estimator	32
4.1.1	Estimator Performance	32
4.1.2	Heart Rate and Energy Expenditure Correlation	36
4.2	Van der pol estimator	39
4.2.1	Estimator Performance	39
4.2.2	Correlations with heart rate and energy expenditure	42
4.2.3	IPAQ and Gender correlation	46
5	Discussion	49
5.1	Model performances	49
5.1.1	The double pendulum estimator	49
5.1.2	The van der pol estimator	50
5.2	Correlations with heart rate and energy expenditure	50
5.3	Correlations with demographic variables	50
5.4	Model Generalizability	50
5.5	Further Research	51
6	Concluding remarks	52
	Bibliography	53
A	Additional Material	56
A.1	Power series of the Van der Pol limit cycle	56
A.1.1	Order zero	56
A.1.2	Order one	56
A.1.3	Order two	57
A.1.4	Order three	58
A.2	Atan2	59
A.3	Plots	60
A.3.1	Double pendulum estimator correlations with HR and EE	60
A.3.2	K and ε correlations with IPAQ and Gender	62

Figures

1.1	Experiment process in one test day.	2
2.1	A phase portrait of the limit cycles of the Van der Pol oscillator, (Widdma, n.d.)	5
2.2	The unforced double pendulum	9
3.1	Body markers tracked by the Qualisys motion capture system.	16
3.2	Motion captured trajectories of a wheelchair user during a submax stage	17
3.3	Motion captured trajectories of a wheelchair user during a submax stage, where the shoulder, elbow and hand trajectories have been isolated.	18
3.4	Demonstration on how the data the lengths and angles from the data are calculated.	19
3.5	Measured upper arm and forearm lengths in two dimensions over time.	20
3.6	Motion captured trajectories of a wheelchair user during a submax stage, where the shoulder, elbow and hand trajectories have been isolated.	21
3.7	Phase portrait of \tilde{x} and $\dot{\tilde{x}}$	22
3.8	Heart rate and energy expenditure over time, from the second interval stage at the 2.5% incline test day.	23
3.9	The forced and damped double pendulum	24
3.10	RMSE between approximated limit cycles and the RK4 solution.	28
3.11	Phase portraits of the third order approximations and RK4 solutions of the limit cycle.	28
3.12	RMSE between approximated limit cycles and the RK4 solution.	29
3.13	Phase portraits of the second order approximations and RK4 solutions of the limit cycle.	29
3.14	Phase portrait and sample distribution from $(\tilde{x}, \dot{\tilde{x}})^+$	30
4.1	The worst performance of the simulated model with estimated parameters.	34
4.2	Average performance of the simulated model with estimated parameters.	35
4.3	The best performance of simulated model with estimated parameters.	36
4.4	Explained variance from each principal component with plot of cumulative explained variance.	37
4.5	Correlation loadings heatmap between the parameters of λ and the principal components.	37
4.6	Scatter plot from the 0.5% incline test day of the first principal component against energy expenditure and heart rate. The center of the clusters from each stage are marked as squares.	38

4.7 Scatter plot from the 0.5% incline test day of the second principal component against energy expenditure and heart rate. The center of the clusters from each stage are marked as squares. 38

4.8 The observed values from $(\tilde{x}, \dot{\tilde{x}})^+$ plotted with the estimated values from $\hat{K}f_{[2]}^{(+)}(\tilde{x}, \hat{\varepsilon})$ with the worst FIT values. 40

4.9 The observed values from $(\tilde{x}, \dot{\tilde{x}})^+$ plotted with the estimated values from $\hat{K}f_{[2]}^{(+)}(\tilde{x}, \hat{\varepsilon})$ with average FIT values. 41

4.10 The observed values from $(\tilde{x}, \dot{\tilde{x}})^+$ plotted with the estimated values from $\hat{K}f_{[2]}^{(+)}(\tilde{x}, \hat{\varepsilon})$ with the best FIT values. 41

4.11 The correlation loadings shows the correlation between the estimated values of K and ε and the principal components. 42

4.12 Scatter plot from the 0.5% incline test day of the first principal component against energy expenditure and heart rate. The center of the clusters from each stage are marked as squares. 43

4.13 Scatter plot from the 2.5% incline test day of the first principal component against energy expenditure and heart rate. The center of the clusters from each stage are marked as squares. 43

4.14 Scatter plot from the 5.0% incline test day of the first principal component against energy expenditure and heart rate. The center of the clusters from each stage are marked as squares. 44

4.15 Scatter plot from the 0.5% incline test day of the first principal component against energy expenditure and heart rate. The center of the clusters from each stage are marked as squares. 45

4.16 Scatter plot from the 2.5% incline test day of the first principal component against energy expenditure and heart rate. The center of the clusters from each stage are marked as squares. 45

4.17 Scatter plot from the 5.0% incline test day of the first principal component against energy expenditure and heart rate. The center of the clusters from each stage are marked as squares. 46

4.18 K and ε from the elbow data for all participants during the 0.5% test day with IPAQ levels marked as HIGH or MOD (moderate). 47

4.19 K and ε from the elbow data for all participants during the 0.5% test day with gender marked as M for male and F for female. 48

A.1 Phase portraits of the third order approximations and RK4 solutions of the limit cycle. 60

A.2 Phase portraits of the third order approximations and RK4 solutions of the limit cycle. 60

A.3 Scatter plot from the 2.5% incline test day of the first principal component against energy expenditure and heart rate. The center of the clusters from each stage are marked as squares. 61

A.4 Scatter plot from the 2.5% incline test day of the second principal component against energy expenditure and heart rate. The center of the clusters from each stage are marked as squares. 61

A.5 K and ε from all participants during the 2.5% test day with IPAQ levels marked as HIGH or MOD (moderate). 62

A.6	K and ε from all participants during the 5.0% test day with IPAQ levels marked as HIGH or MOD (moderate).	63
A.7	K and ε from all participants during the 2.5% test day with gender marked as M for male and F for female.	64
A.8	K and ε from all participants during the 5.0% test day with gender marked as M for male and F for female.	65

Tables

1.1	Experiment information describing incline and speed combinations for each test day.	3
4.1	Double pendulum FIT distributions.	33
4.2	Double pendulum MSE distributions.	33
4.3	Van der pol estimator FIT distributions.	39
4.4	Van der pol estimator MSE distributions.	40

Chapter 1

Introduction

1.1 Motivation and Background

Physical activity is related to many physiological and psychological benefits. For example, physical activity plays a vital role in the management of mild-to-moderate mental health diseases (Paluska and Schwenk, 2000) and is associated with a marked decrease in cardiovascular and all-cause mortality in both men and women (Fagard and Cornelissen, 2007), (Nocon et al., 2008).

According to the World Health Organization, 65 million people in the world use a wheelchair as their primary mode of ambulation (World Health Organization, 2008). The majority of these wheelchair users have a lifestyle without much physical activity. In this population, the risk of suffering from at least one of the numerous consequences of physical inactivity is threefold. These consequences include obesity, diabetes, cardiovascular diseases, and some types of cancer (Wilby, 2019). Accordingly, the annual healthcare costs for people who use a wheelchair due to a spinal cord injury range between 17.000 to 28.000 USD per individual (French et al., 2007). Regular physical activity and an active lifestyle are among the best measures to counteract the chronic illnesses mentioned and reduce the massive healthcare-related costs. In this context, physical activity monitoring provides unique possibilities to facilitate healthy behaviors and compliance with physical activity programs and measure the effectiveness of physical activity promotion programs. However, despite numerous attempts by different research groups and private companies, quantifying physical activity and energy expenditure in wheelchair users still remains a challenge.

1.2 The cross-sectional study

The primary research aim of The Digital Wheelchair Project (digiW) is to develop and validate a concept for estimating energy expenditure (EE) and physical activity (PA) in wheelchair users with different disabilities during rest and free-living activities. This research will provide the basis for reaching the long-term innovation goal of the project; to develop, optimize and patent EE and PA estimation algorithms that can be incorporated into an affordable wearable device for the wheelchair user group, which individuals and future home-based health services could

use to track inactivity and promote a healthy lifestyle (NTNU-Discovery, 2019).

1.2.1 Participants

In the first part of the project, 20 able-bodied participants matched for age and gender will serve as a control group, and in the second part, 20 wheelchair users (10 men and 10 women) will be tested (this thesis is based on the data collected from able-bodied participants)

1.2.2 Test protocol

Testing is performed over three separate days on which data is collected during activities ranging from rest to high-intensity exercise. There is a minimum of 24 hours between the test days to ensure recovery, and the first three test days are scheduled within a three-week period. Prior to the tests, information on the demographic variables (age, body mass, body height, gender, and disability-specific characteristics (type of disability, if they had a spinal cord injury; injury level and ASIA score (Kirshblum et al., 2011)) will be registered. An International Physical Activity Questionnaire (IPAQ) is completed to determine the participants' physical activity levels (Craig et al., 2003). Data is then collected during rest (lying and seated) and wheelchair propulsion at different speed-incline combinations for test days 1-3 as shown in figure 1.1 and table 1.1. Participants will also have a 5-minute warm-up and setup-familiarization in the wheelchair between the resting and propulsion measurements on all test days. The order of the test days, which each target one incline (either 0.5, 2.5, and 5% incline), will be counterbalanced. The speeds at each incline have been selected to cover three 4 min bouts from low to high intensity (assessed through blood lactate measurements and heart rate). An incremental test will be conducted at the end of the 2.5% incline day, with a speed increment every minute at a set incline as shown in table 1.1. When the participant is unable to keep up and hits the back of the treadmill, the speed is reduced 1 stage, and the incremental test continues unchanged until exhaustion or steady-state VO_2 .

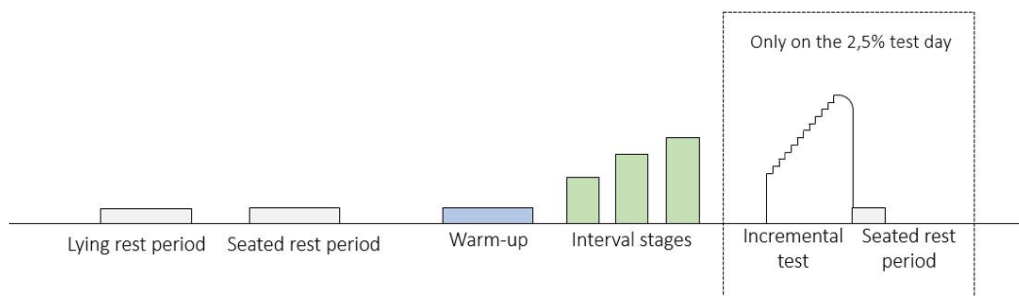


Figure 1.1: Experiment process in one test day.

Stages	0.5%		2.5%		5.0%	
	Men	Women	Men	Women	Men	Women
1	4 km/h	3 km/h	3 km/h	2 km/h	2 km/h	1 km/h
2	6 km/h	5 km/h	4 km/h	3 km/h	3 km/h	2 km/h
3	8 km/h	7 km/h	5 km/h	4 km/h	4 km/h	3 km/h
Incremental			Start at 3 km/h			
			1 km/h increase	0.5 km/h increase		

Table 1.1: Experiment information describing incline and speed combinations for each test day.

1.2.3 Equipment

Heart rate monitor, inertial measurement unit (IMU, accelerometer including gyroscope and magnetometer), Vyntus CPX/portable Metamax II (Metamax, [n.d.](#)), existing wearable devices (Fitbit and Apple) and a Qualisys motion capture system (Qualisys, [n.d.](#)) are used to track/monitor physical activity.

1.3 Scope and Research Objectives

In this thesis, we will focus specifically on the interval stages completed by the participants on each test day. We will try to fit different mathematical models to the motion-captured trajectories from the participants and analyze how these trajectories are connected with heart rate, energy expenditure, and other demographic variables provided by the participants. The approach to this problem is made from a control engineering perspective; consequently, the analysis is based upon trying to explain the motion-captured trajectories as dynamical systems. The oscillating properties of the motion-captured trajectories will be modeled using known relaxation-oscillators, and a simplified mathematical model of the human arm will be used to analyze the arm movement trajectories.

Primary Objective: Provide an analysis upon whether motion captured trajectories of wheelchair users correlate with heart rate and energy expenditure.

Secondary Objectives:

- Present an analysis on whether the models derived can be generalized amongst the participants.
- Examine how different interval stages and/or inclines impact the precision of the models.
- Provide an analysis on whether some of the demographic variables serve as indicators on the properties of the motion captured trajectories.

Chapter 2

Theory

In this section, we provide the theoretical basis for our study.

In order to model the motion-captured trajectories, we have chosen to use the Van der Pol oscillator and the double pendulum as our mathematical models. The Van der Pol oscillator has a long history of being used to explain oscillatory behavior in both physical and biological sciences (FitzHugh, 1961), (Nagumo et al., 1962). Therefore, we aim to investigate if there is similar behavior in the oscillatory movements of the participants and the Van der Pol oscillator. Furthermore, the double pendulum has also seen applications in modeling the human arm as a dynamical system (Agarana and Akinlabi, 2018), (Bieda and Jaskot, 2018). Hence we will try to derive a simplified model of the human arm based upon the double pendulum to model the motion-captured trajectories.

2.1 The Van der Pol unforced oscillator

We consider the non-linear second order *ordinary differential equation*(ODE)

$$\ddot{x} - \varepsilon(1 - x^2)\dot{x} + x = 0, \quad (2.1)$$

where

$$x \equiv x(t) \quad (2.2)$$

is the unknown real function of time, where $x : \mathbb{R} \rightarrow \mathbb{R}$ is twice continuously differentiable i.e $x \in C^2(\mathbb{R})$ and $\varepsilon \in \mathbb{R}$ is a constant control parameter.

We now write the second order equation described in equation (2.1) as two coupled first order ODEs,

$$\begin{cases} \dot{x} = y \\ \dot{y} = \varepsilon(1 - x^2)y - x \end{cases} \quad (2.3)$$

As the system described in equation (2.3) is *autonomous* it can be replaced by an *equation of integral curves* where $y \neq 0$, given as

$$y' = \varepsilon(1-x^2) - \frac{x}{y} \iff yy' = \varepsilon(1-x^2)y - x. \quad (2.4)$$

where

$$y \equiv y(x) \text{ and } y' = \frac{d}{dx}y$$

In order to proceed analytically we need to approximate $y(x)$ since we are not able integrate to find a solution (Strumia, 2018).

2.1.1 The limit cycle of the Van der Pol oscillator

The Van der Pol oscillator is a *relaxation-oscillator*, meaning it has a stable limit cycle. In practice this means that given any initial condition, all trajectories will approach the limit cycle when $t \rightarrow \infty$. The limit cycles from different ε values are depicted in the phase portrait of x and \dot{x} in figure 2.1.

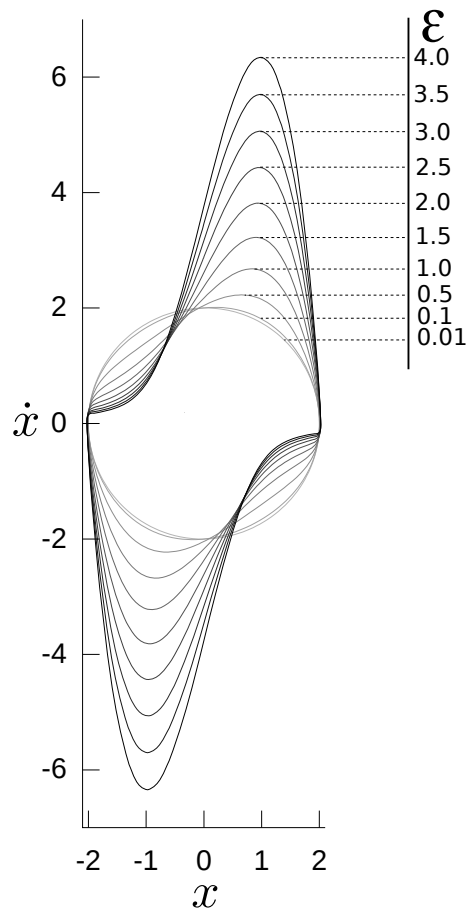


Figure 2.1: A phase portrait of the limit cycles of the Van der Pol oscillator, (Widdma, n.d.)

The stable limit cycle of the Van der Pol oscillator exists in $x \in [-2, 2]$ and $\dot{x} \in \mathbb{R}$.

2.1.2 Power expansion with respect to ε

In this section we will look for approximate analytical solutions of equation (2.4) through a power expansion of the control parameter ε . Consider the Taylor expansion

$$f(x) = \sum_{k=0}^{\infty} h_k(x) \varepsilon^k \quad (2.5)$$

which under the assumption that $\varepsilon \ll 1$, is convergent. However, we may drop higher order contributions according to the desired order of approximation, n regardless of the assumptions on the series convergence. So we consider the Taylor polynomial

$$f_{[n]}(x) = h_0(x) + h_1(x)\varepsilon + h_2(x)\varepsilon^2 + \dots + h_n(x)\varepsilon^n, \quad (2.6)$$

which is to be introduced into the differential equation:

$$p(x, \varepsilon) \equiv f(x) \frac{df(x)}{dx} - \varepsilon(1-x^2)f(x) + x = 0 \quad (2.7)$$

Further we consider the Taylor expansion of $p(x, \varepsilon)$ at order n , in a neighbourhood of $\varepsilon = 0$

$$p_{[n]}(x, \varepsilon) = p(x, 0) + \frac{\partial p}{\partial \varepsilon}(x, 0)\varepsilon + \frac{1}{2} \frac{\partial^2 p}{\partial \varepsilon^2}(x, 0)\varepsilon^2 + \dots + \frac{1}{n!} \frac{\partial^n p}{\partial \varepsilon^n}(x, 0)\varepsilon^n \quad (2.8)$$

which will be required to be zero.

The power expansion of order zero is calculated to be

$$f_{[0]}^{(\pm)}(x) = \pm \sqrt{4-x^2} \quad (2.9)$$

The power expansion of order one is calculated to be

$$f_{[1]}^{(\pm)}(x, \varepsilon) = \pm \sqrt{4-x^2} + \left(x - \frac{x^3}{4}\right) \varepsilon \quad (2.10)$$

The power expansion of order two is calculated to be

$$f_{[2]}^{(\pm)}(x, \varepsilon) = \pm \sqrt{4-x^2} + \left(x - \frac{x^3}{4}\right) \varepsilon \pm \frac{x^6 - 6x^4 + 32}{96\sqrt{4-x^2}} \varepsilon^2. \quad (2.11)$$

The power expansion of order three is calculated to be

$$\begin{aligned} f_{[3]}^{(\pm)}(x, \varepsilon) = & \pm \sqrt{4-x^2} + \left(x - \frac{x^3}{4}\right) \varepsilon \pm \frac{x^6 - 6x^4 + 32}{96\sqrt{4-x^2}} \varepsilon^2 + \\ & + \left(\frac{\sin^{-1}\left(\frac{x}{2}\right)}{48\sqrt{4-x^2}} - \frac{3x^7 - 22x^5 + 34x^3 + 12x}{2304} \right) \varepsilon^3. \end{aligned} \quad (2.12)$$

More detailed calculations of equations (2.9), (2.10), (2.11) and (2.12) are provided in appendix A.1 (Strumia, 2018).

2.2 Mathematical modelling of the double pendulum

In this section, we go through the necessary theory to describe the mathematical model of the double pendulum.

2.2.1 Lagrangian mechanics

Lagrangian mechanics differ from Newtonian mechanics in a way that it uses the energies of a system compared to the forces. The central quantity of Lagrangian mechanics is the *Lagrangian*, which is a function that summarizes the dynamics of the entire system. The *non-relativistic* Lagrangian for a system of particles can be defined as

$$\mathcal{L} = T - V \quad (2.13)$$

where T is the kinetic energy and V is the potential energy.

The total kinetic energy of the system is given by

$$T = \frac{1}{2} \sum_{i=1}^N m_i \|\dot{p}_i\|^2 = \frac{1}{2} \sum_{i=1}^N m_i \dot{p}_i^\top \dot{p}_i \quad (2.14)$$

where p_i is a punctual mass whose position is fixed with respect to a reference frame given by $p \in \mathbb{R}^D$, where D is the number of dimensions.

The potential energy of the system reflects the energy of interaction between particles, i.e. how much energy one particle will have due to the others and other external influences. The potential energy is always a function of the particles position,

$$V = V(p_1, p_2, \dots) \quad (2.15)$$

We define the generalized coordinates of a system as a vector of time-varying coordinates $\mathbf{q}(t) \in \mathbb{R}^{n_c}$ that must be able to describe the "configuration" of the system at a given time t . The generalized coordinates typically gather positions and angles, but can also include more abstract representations of the system. If a system has the generalized coordinates q , then its position p is a function of q . The mass velocity \dot{p} is then a direct result of the chain rule;

$$\dot{p} = \frac{\partial p}{\partial q} \dot{q} \quad (2.16)$$

Furthermore the kinetic energy can be rewritten with respect to q as

$$T = \frac{1}{2} \sum_{i=1}^N m_i \dot{p}_i^\top \dot{p}_i = \frac{1}{2} \sum_{i=1}^N m_i \dot{q}^\top \frac{\partial p_i^\top}{\partial q} \frac{\partial p_i}{\partial q} \dot{q} = \frac{1}{2} \dot{q}^\top \left(\sum_{i=1}^N m_i \frac{\partial p_i}{\partial q} \frac{\partial p_i}{\partial q} \right) \dot{q} \quad (2.17)$$

where we can define

$$W = \sum_{i=1}^N m_i \frac{\partial p_i}{\partial q} \frac{\partial p_i}{\partial q} \quad (2.18)$$

where W is a *semi-positive definite* square matrix. Generally, the kinetic energy function will take the form:

$$T(q, \dot{q}) = \frac{1}{2} \dot{q}^\top W(q) \dot{q} \quad (2.19)$$

With rewriting the potential energy with respect to q we can write the Lagrange function from equation (2.13) as the following:

$$\mathcal{L}(q, \dot{q}) = \frac{1}{2} \dot{q}^\top W(q) \dot{q} - V(q) \quad (2.20)$$

The Euler-Lagrange equation then reads as:

$$\frac{d}{dt} \frac{\partial \mathcal{L}}{\partial \dot{q}} - \frac{\partial \mathcal{L}}{\partial q} = 0 \quad (2.21)$$

which defines the model of the mechanical system (Gros, 2021).

2.2.2 External forces in Lagrangian mechanics

The Lagrangian modelling approach is intrinsically an energy-based point of view of the mechanical system. As a result in the Lagrange approach, the external forces and moments must be considered in terms of the energy they deliver to or remove from the system. In other words, one must consider the work produced on the system by the external forces and moments. Work is related to motions occurring under forces and moments, and motions are described in the Lagrange approach as changes in the generalized coordinates q .

The generalized external forces in the system should satisfy

$$\frac{\partial E}{\partial q} = Q \quad (2.22)$$

where E is the energy and Q is the generalized forces with respect to q .

This concept is often presented in the literature as the following equation

$$\delta W = \langle Q, \delta q \rangle \quad (2.23)$$

where $\langle \cdot, \cdot \rangle$, denotes the inner product space between Q and δq . Here, equation (2.23) is essentially saying the same as in equation (2.22), i.e a "small" motion δq combined with the external forces and moments Q , produces a "small" amount of work δW .

Suppose that a force is given by a vector $F \in \mathbb{R}^n$, where n is the number of dimensions in which we are working in a given reference frame \mathcal{R} is applied to a specific point $p \in \mathbb{R}^n$ in the

same reference frame \mathcal{R} . We then observe that a small change in the generalized coordinates q yields a small displacement of the position p given by the Jacobian $\frac{\partial p}{\partial q}$, and a small work

$$\delta W = F^\top \frac{\partial p}{\partial q} \delta q \quad (2.24)$$

It follows that in this case the generalized force corresponding to F is given by

$$Q = \frac{\partial p^\top}{\partial q} F \quad (2.25)$$

which can be included in the Lagrange formalism using the Euler-Lagrange equation from equation (2.21) as

$$\frac{d}{dt} \frac{\partial \mathcal{L}}{\partial \dot{q}} - \frac{\partial \mathcal{L}}{\partial q} = Q \quad (2.26)$$

(Gros, 2021)

2.2.3 The dynamics of the double pendulum

Consider the double pendulum shown in figure 2.2. The double pendulum is formed by attaching a pendulum directly onto another one. Each pendulum consists of one mass m connected to a massless rigid rod with length l . The forces acting on the masses of the unforced double pendulum are the tensions T and the gravitational forces mg .

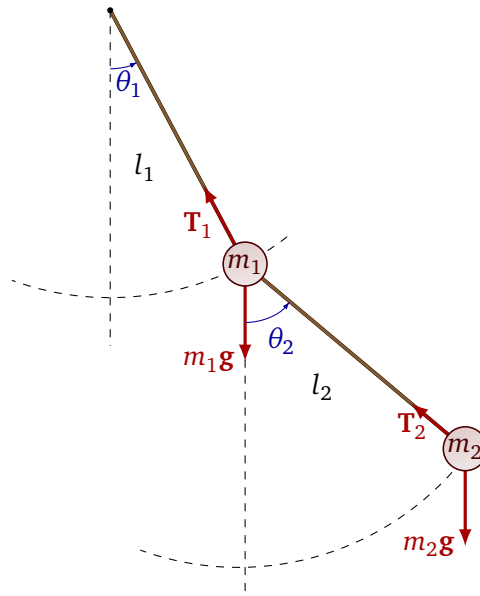


Figure 2.2: The unforced double pendulum

We consider the reference frame \mathcal{R} , of which the double pendulum exists in as a two dimensional cartesian coordinate system (x, y) , with the origin placed at the pivot point of the upper pendulum.

To describe the system in a Lagrangian framework, we begin with defining the general coordinates of the system

$$\mathbf{q} = \begin{bmatrix} \theta_1 \\ \theta_2 \end{bmatrix} \quad (2.27)$$

as it is simple and describes the "configuration" of the system.

We proceed with describing the positions \mathbf{p} , of the two masses as a function of the generalized coordinates.

Where the cartesian position of the upper mass m_1 , can be described as

$$\mathbf{p}_1 = R(\theta_1) \begin{bmatrix} 0 \\ -l_1 \end{bmatrix} = \begin{bmatrix} l_1 \sin \theta_1 \\ -l_1 \cos \theta_1 \end{bmatrix} \quad (2.28)$$

where

$$R(\theta_1) = \begin{bmatrix} \cos \theta_1 & -\sin \theta_1 \\ \sin \theta_1 & \cos \theta_1 \end{bmatrix} \quad (2.29)$$

The lower mass m_2 , has the cartesian position

$$\mathbf{p}_2 = \mathbf{p}_1 + R(\theta_2) \begin{bmatrix} 0 \\ -l_2 \end{bmatrix} = \begin{bmatrix} l_1 \sin \theta_1 + l_2 \sin \theta_2 \\ -l_1 \cos \theta_1 - l_2 \cos \theta_2 \end{bmatrix} \quad (2.30)$$

The kinetic energy function $T(\mathbf{q})$, reads as

$$T(\mathbf{q}) = \frac{1}{2} \sum_{k=1}^2 m_k \dot{\mathbf{p}}_k^\top \dot{\mathbf{p}}_k \quad (2.31)$$

Using both equation (2.16) and equation (2.17) we can describe the kinetic energy as a function of the general coordinates.

$$T(\mathbf{q}) = \frac{1}{2} \dot{\mathbf{q}}^\top W(\mathbf{q}) \dot{\mathbf{q}} \quad (2.32)$$

Using equation (2.18) we compute $W(\mathbf{q})$ to be

$$W(\mathbf{q}) = \begin{bmatrix} (m_1 + m_2)l_1^2 & m_2 l_1 l_2 \cos(\theta_1 - \theta_2) \\ m_2 l_1 l_2 \cos(\theta_1 - \theta_2) & l_2^2 \end{bmatrix} \quad (2.33)$$

The potential energy function $V(\mathbf{q})$ is given by

$$V(\mathbf{q}) = g \sum_{k=1}^2 m_k \mathbf{p}_{k,2} = -(m_1 + m_2)gl_1 \cos \theta_1 - m_2 gl_2 \cos \theta_2 \quad (2.34)$$

where $\mathbf{p}_{k,2}$ denotes the "y-coordinate" of the position \mathbf{p}_k with respect to \mathcal{R} .

Now we can formulate the Lagrangian and the Euler-Lagrange equation respectively as

$$\mathcal{L}(\mathbf{q}, \dot{\mathbf{q}}) = \frac{1}{2} \dot{\mathbf{q}}^\top W(\mathbf{q}) \dot{\mathbf{q}} - V(\mathbf{q}) \quad (2.35)$$

and

$$\frac{d}{dt} \nabla_{\dot{\mathbf{q}}} \mathcal{L} - \nabla_{\mathbf{q}} \mathcal{L} = 0 \quad (2.36)$$

where we use gradient notation i.e

$$\nabla_{\dot{\mathbf{q}}} \mathcal{L} = \frac{\partial \mathcal{L}^\top}{\partial \dot{\mathbf{q}}}, \quad \nabla_{\mathbf{q}} \mathcal{L} = \frac{\partial \mathcal{L}^\top}{\partial \mathbf{q}} \quad (2.37)$$

We can then compute

$$\begin{aligned} \nabla_{\dot{\mathbf{q}}} \mathcal{L} &= W(\mathbf{q}) \dot{\mathbf{q}} \\ \frac{d}{dt} \nabla_{\dot{\mathbf{q}}} \mathcal{L} &= W(\mathbf{q}) \ddot{\mathbf{q}} + \frac{\partial}{\partial \mathbf{q}} (W(\mathbf{q}) \dot{\mathbf{q}}) \dot{\mathbf{q}} \\ \nabla_{\mathbf{q}} \mathcal{L} &= \begin{bmatrix} -m_2 l_1 l_2 \dot{\theta}_1 \dot{\theta}_2 \sin(\theta_1 - \theta_2) - (m_1 + m_2) g l_1 \sin \theta_1 \\ m_2 l_1 l_2 \dot{\theta}_1 \dot{\theta}_2 \sin(\theta_1 - \theta_2) - m_2 g l_2 \sin \theta_2 \end{bmatrix} \end{aligned} \quad (2.38)$$

where

$$\frac{\partial}{\partial \mathbf{q}} (W(\mathbf{q}) \dot{\mathbf{q}}) \dot{\mathbf{q}} = m_2 l_1 l_2 \begin{bmatrix} -\dot{\theta}_1 \dot{\theta}_2 \sin(\theta_1 - \theta_2) + \dot{\theta}_2^2 \sin(\theta_1 - \theta_2) \\ -\dot{\theta}_1^2 \sin(\theta_1 - \theta_2) + \dot{\theta}_1 \dot{\theta}_2 \sin(\theta_1 - \theta_2) \end{bmatrix} \quad (2.39)$$

We can now assemble the model in its explicit form by rearranging the Euler-Lagrange equation from equation (2.36):

$$\ddot{\mathbf{q}} = W(\mathbf{q})^{-1} \left[\nabla_{\mathbf{q}} \mathcal{L} - \frac{\partial}{\partial \mathbf{q}} (W(\mathbf{q}) \dot{\mathbf{q}}) \dot{\mathbf{q}} \right] \quad (2.40)$$

However, the model in equation (2.40) is a second order ordinary differential equation. To be able to use a numerical method to solve this equation we have to formulate the model as a system of first order ordinary differential equations. We do this by introducing the state vector, $\mathbf{x} \in \mathbb{R}^4$, where

$$\mathbf{x} = \begin{bmatrix} \mathbf{q} \\ \boldsymbol{\omega} \end{bmatrix}, \quad \boldsymbol{\omega} = \begin{bmatrix} \dot{\theta}_1 \\ \dot{\theta}_2 \end{bmatrix} \quad (2.41)$$

Now we can write the model as a system of coupled first order ordinary differential equations:

$$\dot{\mathbf{x}} = \begin{bmatrix} \dot{\mathbf{q}} \\ \dot{\boldsymbol{\omega}} \end{bmatrix} = \begin{bmatrix} W(\mathbf{q})^{-1} \left[\nabla_{\mathbf{q}} \mathcal{L} - \frac{\partial}{\partial \mathbf{q}} (W(\mathbf{q}) \boldsymbol{\omega}) \boldsymbol{\omega} \right] \end{bmatrix} \quad (2.42)$$

which fully explains the dynamics of the unforced double pendulum (Bogdanov, 2004).

2.3 Numerical methods for solving ODEs

We make use of numerical methods in order to be able to validate the analytical approximations of the Van der Pol oscillator from section 2.1.2 and to solve the initial value problem of the nonlinear ODE describing the double pendulum from section 2.2.3. The Runge-Kutta method described is generally a robust and precise numerical ODE solver, however as shown in (Chen, 2008) an Adams-Moulton style method might be better for solving the initial value problem of the double pendulum.

2.3.1 Runge-Kutta 4

The most widely used and known Runge-Kutta method is the fourth order Runge-Kutta method (RK4). The method can be used to give a discrete approximate solution to ordinary differential equations. Let an initial value problem be specified as

$$\frac{dy}{dt} = f(t, y), \quad y(t_0) = y_0 \quad (2.43)$$

For some $h > 0$, the RK4 method reads as follows.

$$\begin{aligned} y_{n+1} &= y_n + \frac{1}{6}h(k_1 + 2k_2 + 2k_3 + k_4) \\ t_{n+1} &= t_n + h \end{aligned} \quad (2.44)$$

for $n = 0, 1, 2, 3, \dots$ where

$$\begin{aligned} k_1 &= f(t_n, y_n), \\ k_2 &= f\left(t_n + \frac{h}{2}, y_n + h\frac{k_1}{2}\right), \\ k_3 &= f\left(t_n + \frac{h}{2}, y_n + h\frac{k_2}{2}\right), \\ k_4 &= f(t_n + h, y_n + hk_3). \end{aligned} \quad (2.45)$$

(Butcher, 2016a).

2.3.2 Adams–Moulton methods

The Adams–Moulton method is an implicit linear multistep method. Methods such as the Runge kutta methods take some intermediate steps (for example, a half-step) to obtain a higher order method, but then discard all previous information before taking a second step. Linear multistep methods, on the other hand, attempt to gain efficiency by keeping and using the information from previous steps rather than discarding it. The Adams-Moulton methods of order $s = 0, 1, 2, \dots$ reads as

$$\begin{aligned}
 y_n &= y_{n-1} + hf(t_n, y_n) \\
 y_{n+1} &= y_n + \frac{1}{2}h(f(t_{n+1}, y_{n+1}) + f(t_n, y_n)) \\
 y_{n+2} &= y_{n+1} + h\left(\frac{5}{12}f(t_{n+2}, y_{n+2}) + \frac{8}{12}f(t_{n+1}, y_{n+1}) - \frac{1}{12}f(t_n, y_n)\right) \\
 &\vdots \\
 y_{n+s} &= y_{n+s-1} + h(\beta_0 f(t_{n+s}, y_{n+s}) + \dots + \beta_s f(t_n, y_n))
 \end{aligned} \tag{2.46}$$

where

$$\beta_{s-j} = \frac{(-1)^j}{j!(s-j)!} \int_0^1 \prod_{\substack{i=0 \\ i \neq j}}^s (u+i-1) du, \quad \text{for } j = 0, \dots, s \tag{2.47}$$

(Butcher, 2016b).

2.4 Least squares estimation

To be able to fit our mathematical models to the data gathered from the participants, we make use of least squares estimation. The method of least squares is about estimating parameters by minimizing the squared discrepancies between observed data, on the one hand, and their expected values on the other. Given a data set $\{(x_i, y_i)\}_{i=1}^n$, where x_i is an independent variable and y_i is a dependent variable whose value is found by observation. The model function has the form $f(x, \boldsymbol{\beta})$, where $\boldsymbol{\beta} \in \mathbb{R}^m$. The least squares method then aims to find the $\boldsymbol{\beta}$ that minimizes

$$\sum_{i=1}^n (y_i - f(x_i, \boldsymbol{\beta}))^2 \tag{2.48}$$

(Van De Geer, 2005)

2.5 Measurements of performance

There are several ways to measure the performance of a model. In this study we will use three methods to evaluate the model parameter estimations in trajectory tracking; mean square error, root mean square error and a version of R^2 we call FIT.

2.5.1 Mean Square Error

The mean square error between a vector of observed values \mathbf{y} and a vector of a predicted or estimated value $\hat{\mathbf{y}}$ is defined as

$$\text{MSE} = \frac{1}{n} \sum_{i=1}^n (y_i - \hat{y}_i)^2 \quad (2.49)$$

2.5.2 Root Mean Square Error

The root mean square error between a vector of observed values \mathbf{y} and a vector of a predicted or estimated value $\hat{\mathbf{y}}$ is defined as square the square root of the mean square error. Using equation (2.49) the root mean square error or RMSE reads as

$$\text{RMSE} = \sqrt{\text{MSE}} \quad (2.50)$$

2.5.3 FIT

The R^2 error between a vector of observed values \mathbf{y} and a vector of a predicted or estimated value $\hat{\mathbf{y}}$ is defined as

$$R^2 = 1 - \frac{\|\mathbf{y} - \hat{\mathbf{y}}\|_2^2}{\|\mathbf{y} - \bar{\mathbf{y}}\|_2^2} \quad (2.51)$$

where $\bar{\mathbf{y}}$ is the mean of the observed values \mathbf{y} .

Then we simply define the FIT as $100 \times R^2$.

2.6 Principal Component Analysis

PCA extracts the most important information from the data and expresses this a new set of orthogonal variables called *principal components* (Abdi and Williams, 2010). This method is very useful to perform dimensionality reduction, i.e capture the variance explained by some data in fewer dimensions. This might prove useful for us when interpreting the parameters estimated, if the parameters are of high dimension, dimensionality reduction may be put to use.

2.6.1 Singular Value Decomposition

The components of PCA are obtained from a *singular value decomposition* (SVD). Given a real valued matrix $X \in \mathbb{R}^{m \times n}$. The singular value decomposition is mathematically defined as

$$X = U \Sigma V^T, \quad (2.52)$$

where U is an $m \times n$ matrix, Σ is an $m \times n$ diagonal matrix, and V^T is an $n \times n$ matrix. The columns of U and V are the *left-singular vectors* and *right-singular vectors* of X , respectively. Both the left- and right-singular vectors form a set of orthonormal vectors, making

the matrices U and V unitary matrices. The matrix Σ contains the *singular values*, σ_i on its diagonal entries. By convention the ordering of the singular vectors in Σ is from the highest singular value to the lowest (Wall et al., 2003).

2.6.2 Derivation of PCA through singular value decomposition

Given some data set $X \in \mathbb{R}^{m \times n}$ with mean centered columns. Then the $n \times n$ covariance matrix C is given by $C = X^T X / (n - 1)$ and has the eigendecomposition

$$C = P L P^T \quad (2.53)$$

where P is a matrix of eigenvectors and L is a diagonal matrix containing the eigenvalues λ_i in decreasing order on the diagonal. The eigenvectors of P are called *principal axes* of X . Projecting the data, X on the principal axes are called *principal components* or *scores* often denoted as T , given by the projection, $T = X P$.

If we perform a singular value decomposition on X , we obtain $X = U \Sigma V^T$ as defined in equation 2.52. We can now write the correlation matrix, C as

$$C = \frac{X^T X}{n - 1} = \frac{V \Sigma U^T U \Sigma V^T}{n - 1} = V \frac{\Sigma^2}{n - 1} V^T \quad (2.54)$$

showing that the right-singular vectors V are the eigenvectors or *principal axes* of the covariance matrix, C and that the singular values of X are given from the eigenvalues of the covariance matrix, C through $\lambda_i = \sigma_i^2 / (n - 1)$. Furthermore the scores, T are given as $T = X V = U \Sigma V^T V = U \Sigma$, giving us

$$X = U \Sigma V^T \Rightarrow X = T P^T \quad (2.55)$$

where T are the principal components or scores and P are the principal axes. In PCA the *loadings* are the principal axes multiplied by square root of corresponding eigenvalues.

2.6.3 Dimensionality Reduction

Given a real valued matrix $X \in \mathbb{R}^{m \times n}$ where $X = T P^T$. PCA can also be written on vector form as

$$X = t_1 p_1^T + t_2 p_2^T + \dots + E \quad (2.56)$$

where one could choose a specific amount components to explain the data set X , eg.

$$\hat{X} = \sum_{a=1}^A t_a p_a^T, A < n \quad (2.57)$$

Since the variance the singular values in Σ are in descending order, the first components explain the most variance. And the "essence" of X can be captured by the first few components.

Chapter 3

Method and set-up

This section provides insight into the specifics of our problem and how we will solve it. In addition, this section contains the necessary processing methods to use our data as planned. Moreover, the section contains a detailed description of the derivation of our estimators.

3.1 Motion trajectories

The motion trajectory data of the wheelchair users participating in this study is provided from a Qualisys motion capture system. The markers tracked by the Qualisys motion capture system are attached to the wheelchair users per figure 3.1.

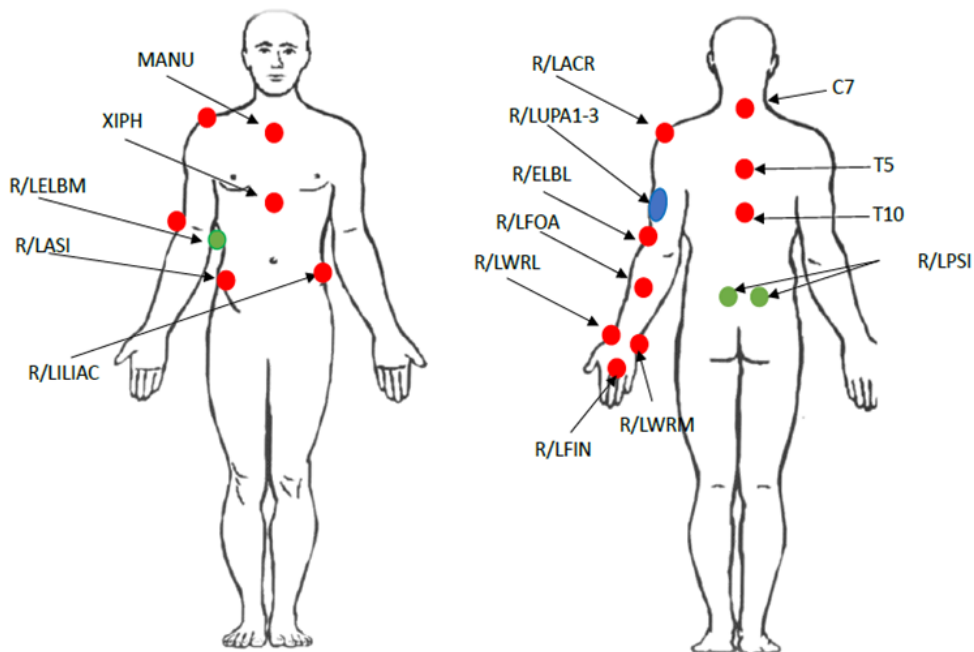


Figure 3.1: Body markers tracked by the Qualisys motion capture system.

Furthermore, four markers are placed on the wheelchair itself, where one pair is placed on the shaft of each wheel, and the other pair is placed on the rim of each wheel, making it a total of 33 markers tracked by the Qualisys motion capture system.

The movement of these markers is tracked with a frequency of $f = 120\text{Hz}$ and makes up the trajectories shown in figure 3.2

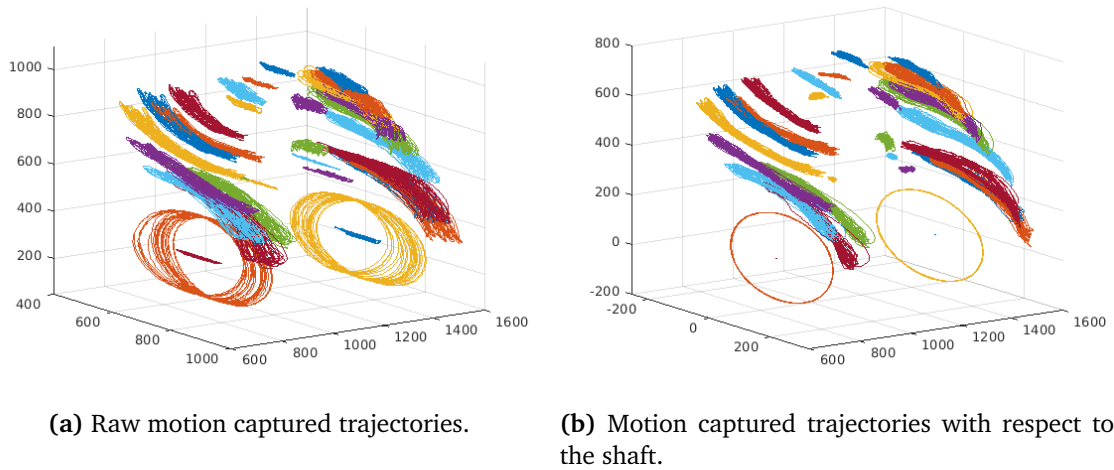


Figure 3.2: Motion captured trajectories of a wheelchair user during a submax stage

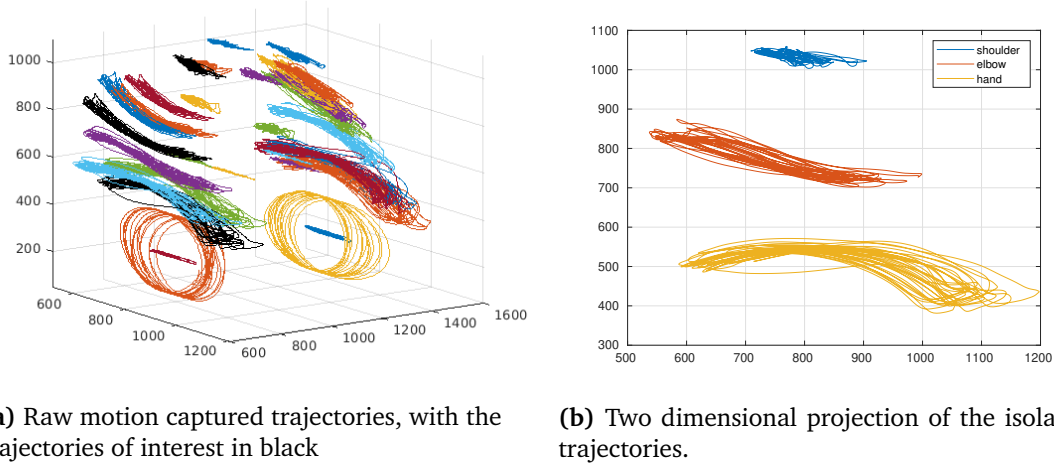
3.2 Energy expenditure

To calculate the energy expenditure ($EE \sim [\text{kJ}/\text{min}]$), values for internal gas exchange, $\dot{V}O_2$ and $\dot{V}CO_2$, will be used. $\dot{V}O_2$ and $\dot{V}CO_2$ are provided from the Vyntus CPX/portable Metamax II measurement system as mentioned in section 1.2.3. Furthermore, the calculation of energy expenditure is based on the corrected Weir formula (Brockway, 1987), with assumed zero protein metabolism (Kipp et al., 2018). The energy expenditure calculation then reads as

$$EE = [16.62 \times \dot{V}O_2 + 4.51 \times \dot{V}CO_2] \times 60 \quad (3.1)$$

3.3 Preprocessing of the data

In this thesis, the most interesting part of the motion-captured data is the trajectories produced by the arm movement. It is from these trajectories we hope to find the correlations between heart rate and energy expenditure measurements. Hence, we move forward with isolating the hand, elbow, and shoulder trajectories of the right arm on each participant as depicted in figure 3.3.



(a) Raw motion captured trajectories, with the trajectories of interest in black

(b) Two dimensional projection of the isolated trajectories.

Figure 3.3: Motion captured trajectories of a wheelchair user during a submax stage, where the shoulder, elbow and hand trajectories have been isolated.

In this study, we will only use trajectories in two dimensions to not overly complicate the study. We do this by simply diminishing the "width" dimension. Furthermore, the information on each participant's handedness is known and concludes that all participants are right-handed. Hence, only the right-hand side of the motion-captured trajectories will be used.

Each trajectory of motion-captured data is represented by a time series of cartesian coordinates and assumes the following shape.

$$\mathbf{d} = \{(x, y)\}_{i=1}^N \quad (3.2)$$

3.3.1 Preprocessing for the double pendulum estimator

When studying the arm as a double pendulum, we want to analyze the movement of the elbow and hand with respect to the shoulder. Let \mathbf{d}_s , \mathbf{d}_e and \mathbf{d}_h denote the trajectories of the shoulder, elbow and hand respectively. Furthermore, we subtract the shoulder trajectories from the elbow and hand trajectories as follows

$$\begin{aligned} \tilde{\mathbf{d}}_e &= \mathbf{d}_e - \mathbf{d}_s \\ \tilde{\mathbf{d}}_h &= \mathbf{d}_h - \mathbf{d}_s \end{aligned} \quad (3.3)$$

The elbow and hand trajectories with respect to the shoulder trajectories as depicted in figure 3.4.

For the pendulum experiment, it is necessary to represent the trajectories in polar coordinates. Generally, polar coordinates take the form (r, θ) , where r denotes the distance from the origin to the coordinate and θ denotes the angle between the ray from the origin through the coordinate and the ray from the origin to $(\infty, 0)$.

To be able to compare the data to the double pendulum model, we define our polar coordinates as depicted in figure 3.4, which shows how the points $(x, y)_e^t$ and $(x, y)_h^t$, from the same timestamp t , are represented in polar coordinates.

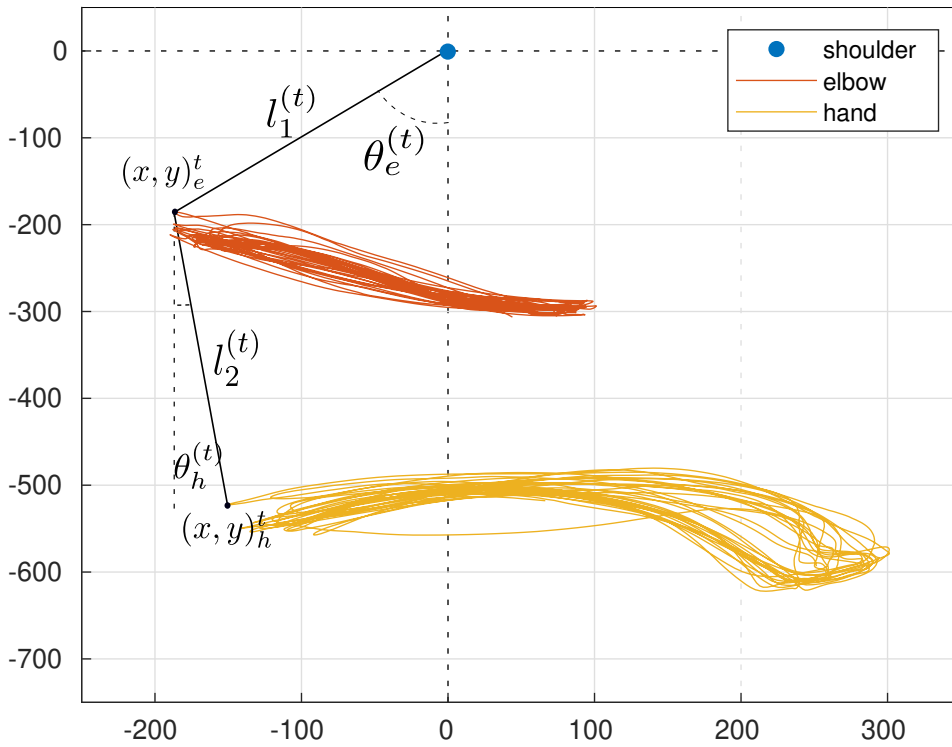


Figure 3.4: Demonstration on how the data the lengths and angles from the data are calculated.

The angles θ_e and θ_h are calculated as follows

$$\begin{aligned}\theta_e &= \text{atan2}(y_e, x_e) + \frac{\pi}{2} \\ \theta_h &= \text{atan2}(y_h - y_e, x_h - x_e) + \frac{\pi}{2}\end{aligned}\tag{3.4}$$

where we are using *atan2* as it is defined in A.2.

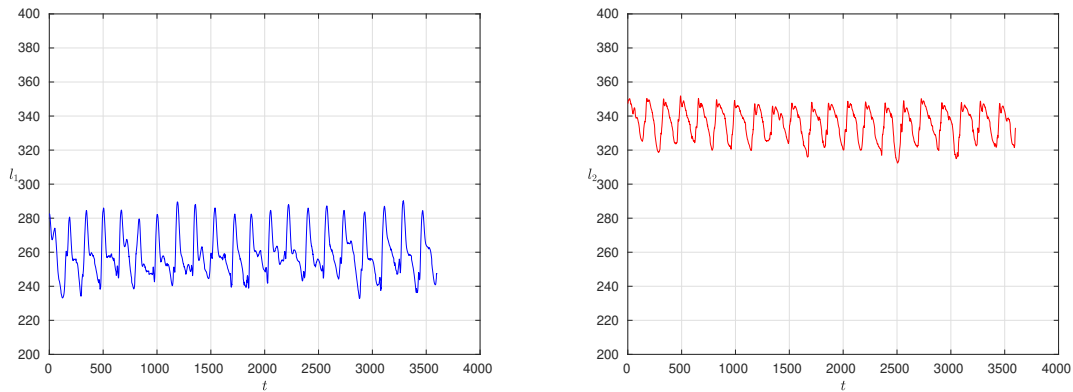
This done for all t , giving us a timeseries of $\boldsymbol{\theta}_e = \{\theta_e\}_{i=1}^N$ and $\boldsymbol{\theta}_h = \{\theta_h\}_{i=1}^N$.

The lengths l_1 and l_2 are calculated as follows

$$\begin{aligned} l_1 &= \sqrt{x_e^2 + y_e^2} \\ l_2 &= \sqrt{(x_h - x_e)^2 + (y_h - y_e)^2} \end{aligned} \quad (3.5)$$

Which is done for all t , giving us a timeseries of $\mathbf{l}_1 = \{l_1\}_{i=1}^N$ and $\mathbf{l}_2 = \{l_2\}_{i=1}^N$.

In the double pendulum model l_1 and l_2 are constants. However this is not the case in the data. Due to hand movements and unaccounted movements in the "width" direction l_1 and l_2 will vary over time. Figure 3.5 shows how l_1 and l_2 develop over time.



(a) Measured upper arm length over time.

(b) Measured forearm length over time.

Figure 3.5: Measured upper arm and forearm lengths in two dimensions over time.

Since there are multiple wheelchair users with different anatomies participating in this study, we choose to generalize the lengths for all participants. This makes it possible to compare the estimated forces from the double pendulum approach between participants without accounting for different arm lengths. However, each participant will still have its own $\frac{l_1}{l_2}$ ratio.

From figure 3.5 we can see that both lengths oscillate between a mean value; hence we move forward using their mean values, and we redefine l_1 and l_2 as follows.

$$\begin{aligned} l_1 &= 1 \\ l_2 &= \frac{\bar{l}_2}{\bar{l}_1} \end{aligned} \quad (3.6)$$

Here, \bar{l}_1 and \bar{l}_2 denotes the mean values of l_1 and l_2 .

The motion trajectories with constant l_1 and l_2 and with varying l_1 and l_2 are depicted in figure 3.6.

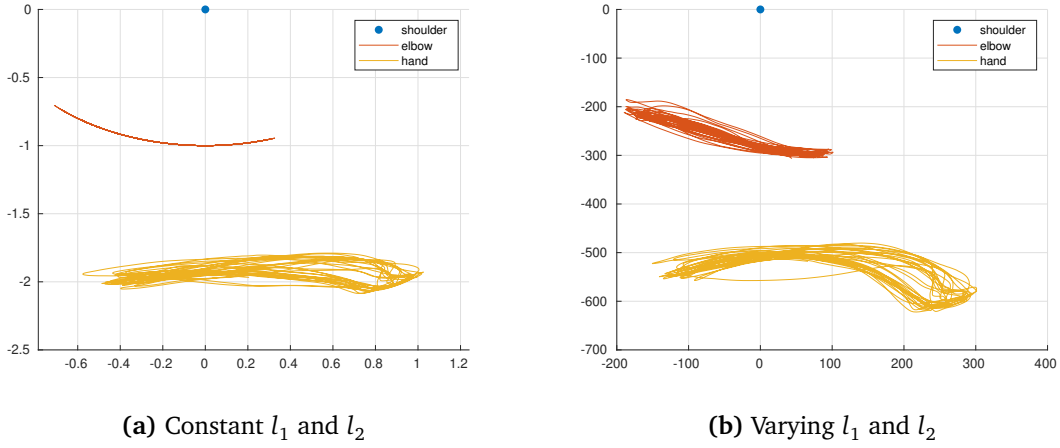


Figure 3.6: Motion captured trajectories of a wheelchair user during a submax stage, where the shoulder, elbow and hand trajectories have been isolated.

3.3.2 Preprocessing for the Van Der Pol estimator

When using the limit cycle of the van der pol oscillator as an estimator, we have to look at the phase portraits of the motion-captured trajectories. In this study, we will only focus on the elbow and hand-tracked trajectories with respect to the shoulder, namely \mathbf{d}_e and \mathbf{d}_h , which is defined in equation (3.3) and depicted as red in figure 3.6b. However, to simplify the problem, we will only work in the horizontal dimension as most of the movement is done in this direction, and the fact that the van der pol oscillator defined in section 2.1 is one dimensional.

Hence we denote the horizontal data from either \mathbf{d}_e or \mathbf{d}_h as

$$\mathbf{x} = \{x\}_{n=1}^N \quad (3.7)$$

In order to make a phase portrait of the horizontal position of the elbow and its speed fit the limit cycle, we need to make sure \mathbf{x} is bounded the same as the limit cycle of the van der pol oscillator is bounded. From section 2.1.1 we have that $x \in [-2, 2]$, hence we scale \mathbf{x} as shown in equation (3.8)

$$\tilde{\mathbf{x}} = -2 + 4 \frac{(x - \min(\mathbf{x}))}{\max(\mathbf{x}) - \min(\mathbf{x})} \quad (3.8)$$

Furthermore, to be able to make a phase portrait of $\tilde{\mathbf{x}}$ and $\dot{\tilde{\mathbf{x}}}$ we need to find the derivative $\dot{\tilde{\mathbf{x}}}$. The time series $\tilde{\mathbf{x}}$ is discrete with a frequency $f = 120\text{Hz}$, hence we define the numerical derivative at each sample $\tilde{\mathbf{x}}[n]$ as

$$\dot{\tilde{\mathbf{x}}}_n = \frac{\tilde{\mathbf{x}}_{n+1} - \tilde{\mathbf{x}}_n}{\Delta t}, \quad \Delta t = \frac{1}{f} \quad (3.9)$$

Now we can make the phase portrait of \tilde{x} and $\dot{\tilde{x}}$ as shown in figure 3.7

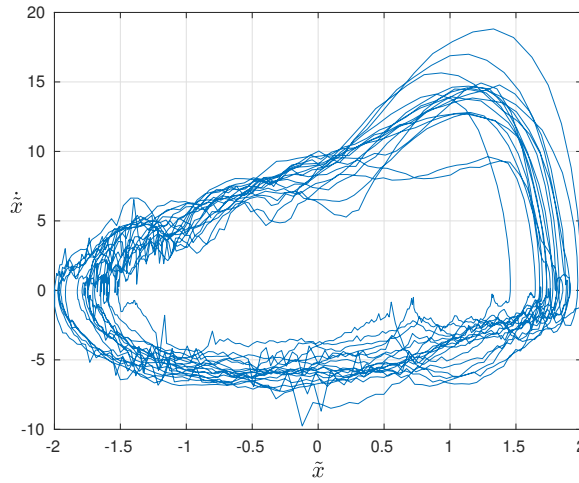


Figure 3.7: Phase portrait of \tilde{x} and $\dot{\tilde{x}}$.

We once more make a simplification by only moving forward with the data points of $(\tilde{x}, \dot{\tilde{x}})$ that satisfies $\dot{\tilde{x}}_n > 0$. Hence we define

$$(\tilde{x}, \dot{\tilde{x}})^+ = \{(\tilde{x}, \dot{\tilde{x}}) : \dot{\tilde{x}}_n > 0\} \quad (3.10)$$

We make this simplification as the analytical solutions f^\pm , of the van der pol oscillator from section 2.1 are piece-wise, i.e $f^+ : [-2, 2] \rightarrow \mathbb{R}^+$ and $f^- : [-2, 2] \rightarrow \mathbb{R}^-$. Furthermore, the part of the trajectories where $\dot{\tilde{x}}_n > 0$ are the trajectories that explain the motion of pushing the arm forward; these trajectories are far more interesting to this study in comparison to the trajectories explaining retraction of the arm.

3.4 Energy expenditure and heart rate centroids

Figure 3.8 shows the heart rate and energy expenditure time series of participants 1 to 3 during the second interval stage from the 2.5% test day.

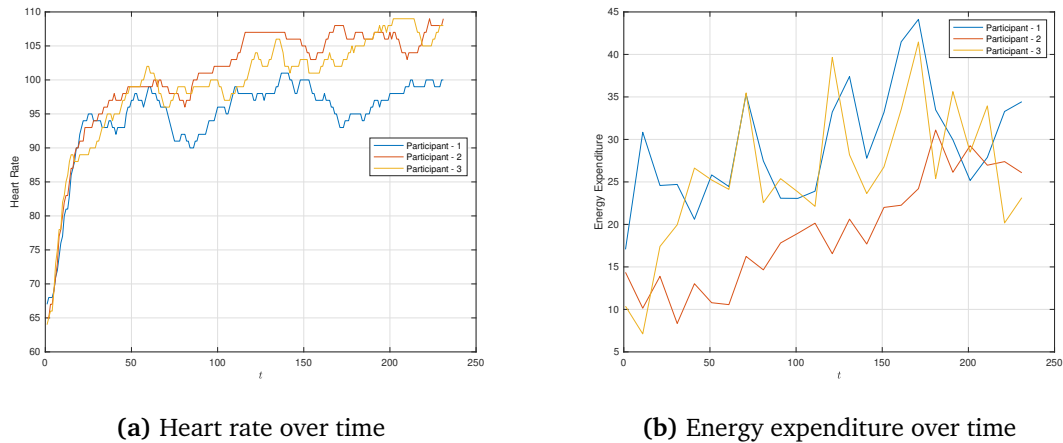


Figure 3.8: Heart rate and energy expenditure over time, from the second interval stage at the 2.5% incline test day.

In order to catch the essence of the heart rate and energy expenditure, we remove the first 60 seconds and the last 30 seconds from the heart rate and energy expenditure signals. We will use centroids of each signal in a steady state to investigate the correlations between heart rate and energy expenditure and the estimated parameters of each model. Therefore, to calculate the heart rate and energy expenditure centroids, we simply take the mean value of the signals in the newly defined interval.

3.5 Modeling of external forces and damping

The autonomous system derived in section 2.2.3 acts as a simplification of the dynamics of the human arm. To further mimic the arm's movements in the wheelchair experiment, some external force must be applied. We picture this force as periodical signals acting on the masses m_1 and m_2 . Furthermore, the forces acting on the wheel from the arm are tangent vectors on the wheel, mainly in the x -direction. Hence, we assume that these forces act horizontally on the masses, i.e., only in the x -direction with respect to \mathcal{R} . The forces F_1 and F_2 acting on the masses m_1 and m_2 are depicted in figure 3.9.

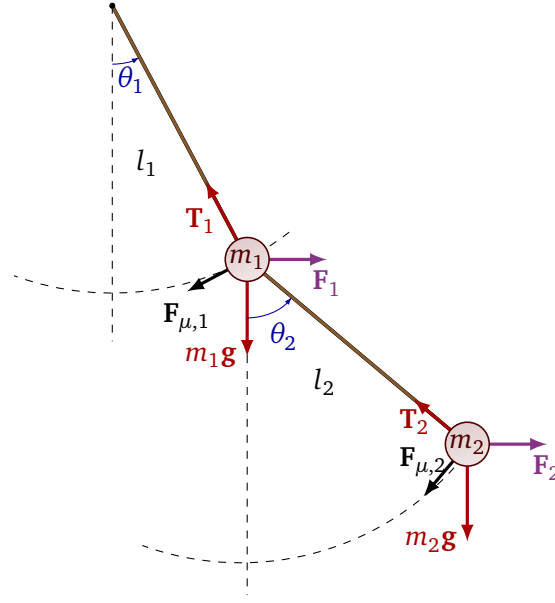


Figure 3.9: The forced and damped double pendulum

We assume that the periodical forces F_1 and F_2 take the form of a square wave as the arm produces a force in the positive x -direction to push the wheel forwards and then a force in the negative x -direction to retract the arm to its starting position. Hence, F_1 and F_2 are defined as

$$\begin{aligned} \mathbf{F}_1 &= \begin{bmatrix} A_1 \operatorname{sgn}(\sin(\Omega_1 t + \phi_1)) + B_1 & 0 \end{bmatrix}^\top \\ \mathbf{F}_2 &= \begin{bmatrix} A_2 \operatorname{sgn}(\sin(\Omega_2 t + \phi_2)) + B_2 & 0 \end{bmatrix}^\top \end{aligned} \quad (3.11)$$

where $\operatorname{sgn}(\cdot)$ is the sign function, A , Ω , ϕ and B are constants and $t \in \mathbb{R}^+$ is time.

Furthermore, the forces F_1 and F_2 must be applied in the Lagrangian framework as described in section 2.2.2. It follows from equation (2.25) that the generalized forces Q_1 and Q_2 corresponding to F_1 and F_2 are given by

$$\mathbf{Q}_1 = \frac{\partial \mathbf{p}_1^\top}{\partial \mathbf{q}} \mathbf{F}_1, \quad \mathbf{Q}_2 = \frac{\partial \mathbf{p}_2^\top}{\partial \mathbf{q}} \mathbf{F}_2 \quad (3.12)$$

where Q_1 and Q_2 are computed to be

$$\mathbf{Q}_1 = \begin{bmatrix} l_1 \cos \theta_1 & l_1 \sin \theta_1 \\ 0 & 0 \end{bmatrix} \mathbf{F}_1, \quad \mathbf{Q}_2 = \begin{bmatrix} l_1 \cos \theta_1 & l_1 \sin \theta_1 \\ l_2 \cos \theta_2 & l_2 \sin \theta_2 \end{bmatrix} \mathbf{F}_2 \quad (3.13)$$

The frictional forces acting on the pendulum work as a dampening effect; they produce a force in the opposite direction of the angular velocities $\dot{\mathbf{q}}$. These forces are introduced to represent the frictional properties of synovial joints in the human arm (G. Stachowiak et al., 1994). Furthermore, we can model the effects of these frictional forces as a moment T working on

the masses m_1 and m_2 in the opposite direction of the angular velocities $\dot{\mathbf{q}}$. This dampening moment can be described as

$$\mathbf{T} = -\zeta \begin{bmatrix} \dot{\theta}_1 \\ \dot{\theta}_2 \end{bmatrix} = -\zeta \dot{\mathbf{q}} \quad (3.14)$$

where $\zeta \sim [\text{kgm}^2/\text{s}]$ is the dampening coefficient.

Here, \mathbf{T} is already described by the generalized coordinates \mathbf{q} and not the fixed reference frame \mathcal{R} which is the case for \mathbf{F}_1 and \mathbf{F}_2 . Hence, we can directly introduce \mathbf{T} into the equations of motion from equation (2.40).

Using equation (2.26) and equation (2.40) we can rewrite the coupled system from equation (2.42) with the external forces \mathbf{Q}_1 , \mathbf{Q}_2 and \mathbf{T} with respect to the state-space $\mathbf{x} = \begin{bmatrix} \mathbf{q} \\ \boldsymbol{\omega} \end{bmatrix}$ as

$$\dot{\mathbf{x}} = \begin{bmatrix} \dot{\mathbf{q}} \\ \dot{\boldsymbol{\omega}} \end{bmatrix} = \begin{bmatrix} \boldsymbol{\omega} \\ W(\mathbf{q})^{-1} \left[\mathbf{Q}_1 + \mathbf{Q}_2 - \zeta \boldsymbol{\omega} + \nabla_{\mathbf{q}} \mathcal{L} - \frac{\partial}{\partial \mathbf{q}} (W(\mathbf{q}) \boldsymbol{\omega}) \boldsymbol{\omega} \right] \end{bmatrix} \quad (3.15)$$

3.6 Estimating F_1 and F_2

Our main objective when estimating the forces F_1 and F_2 is to fit the model described in section 3.5 to the data as best as possible.

First we define the $\boldsymbol{\lambda}$ as the vector containing the parameters we seek to estimate.

$$\boldsymbol{\lambda} = [A \quad \Omega \quad \phi \quad B]^\top \quad (3.16)$$

where $A = [A_1 \quad A_2]$, $\Omega = [\Omega_1 \quad \Omega_2]$, $\phi = [\phi_1 \quad \phi_2]$, $B = [B_1 \quad B_2]$.

We then write our double pendulum model from equation (3.15) as a more compact equation.

$$\dot{\mathbf{x}} = f(t, \mathbf{x}; \boldsymbol{\lambda}), \quad \mathbf{x}(t_0; \boldsymbol{\lambda}) = \mathbf{x}_0 \quad (3.17)$$

Suppose $\mathbf{x}(t; \boldsymbol{\lambda}) = [\hat{\theta}_e(t; \boldsymbol{\lambda}) \quad \hat{\theta}_h(t; \boldsymbol{\lambda}) \quad \hat{\omega}_1(t; \boldsymbol{\lambda}) \quad \hat{\omega}_2(t; \boldsymbol{\lambda})]^\top$ is the solution to equation (3.17) with the initial condition (t_0, \mathbf{x}_0) and $\boldsymbol{\theta}_e$ and $\boldsymbol{\theta}_h$ is the time series from section 3.3.1. We then describe the optimization problem as

$$\min_{\boldsymbol{\lambda}} \sum_{n=1}^N [(\theta_e^{(n)} - \hat{\theta}_e(t_n; \boldsymbol{\lambda}))^2 + (\theta_h^{(n)} - \hat{\theta}_h(t_n; \boldsymbol{\lambda}))^2] \quad (3.18)$$

$$\text{s.t. } \boldsymbol{\lambda} \in \mathcal{O} \quad (3.19)$$

where \mathcal{O} denotes the space that λ is bounded by and the sample n and t_n explains the same point in time. Here, the least squares estimator in equation (3.18) seeks to minimize the difference between the angles from the data and the model.

However, the system in equation (3.17) is a nonlinear ordinary differential equation with no known analytical solution, so we have to solve it numerically with a Runge-Kutta or some other numerical method. This poses a problem as Runge-Kutta methods are iterative, which means that when λ is unknown, the symbolic complexity of the solution will greatly increase for each iteration.

To give an example, if we take the simplest case of a Runge-Kutta method, RK1 or *Euler's Method* and perform it to solve equation (3.17) with an unknown λ , we get the following.

Given the initial value problem of equation (3.17), the Euler method reads as

$$\mathbf{x}_{n+1} = \mathbf{x}_n + hf(t_n, \mathbf{x}_n; \lambda), \quad (3.20)$$

for some step size h .

The first few iterations reads as

$$\begin{aligned} \mathbf{x}_0 &= \mathbf{x}_0 \\ \mathbf{x}_1 &= \mathbf{x}_0 + hf(t_0, \mathbf{x}_0; \lambda) \\ \mathbf{x}_2 &= \mathbf{x}_1 + hf(t_1, \mathbf{x}_1; \lambda) = \mathbf{x}_0 + hf(t_0, \mathbf{x}_0; \lambda) + hf(t_1, \mathbf{x}_0 + hf(t_0, \mathbf{x}_0; \lambda); \lambda) \\ \mathbf{x}_3 &= \dots \end{aligned} \quad (3.21)$$

equation (3.21) clearly shows that with each iteration the symbolic complexity increases massively. This means that in practice, the optimization problem presented in equation (3.18) cannot be solved using derivative-based optimization methods.

We present an objective function that takes in defined values of λ , the known data $\theta = \{\theta_e, \theta_h\}$ and returns the value of some cost function J in algorithm 1.

Algorithm 1 Algorithm of the objective function to minimize

- 1: **function** OBJECTIVEFUNCTION($\lambda, \theta, \mathbf{x}_0, N$)
 - 2: solve $\dot{\mathbf{x}} = f(t, \mathbf{x}, \lambda)$ using a numerical solver for N samples
 - 3: Compute the cost function $J = \|\theta_e - \hat{\theta}_e\|_2^2 + \|\theta_h - \hat{\theta}_h\|_2^2$
 - 4: **return** J
 - 5: **end function**
-

3.6.1 Parameter selection

The constants in the model derived in section 3.5 needs to be defined in order to solve the optimization problem from equation (3.18). The constants that have yet defined are l_1 , l_2 , m_1 , m_2 , ζ and g . Estimates of l_1 and l_2 can be calculated directly from the data as shown in section 3.3.1. However we cannot measure the the masses m_1 and m_2 and the damping constant ζ from the data. From (Plagenhoef et al., 1983), we use the percentages of body

weight measurements *Forearm & Hand* and *Upper Arm* which explains 2.52% and 3.25% of the total body weight respectively. We then define m_1 and m_2 as

$$\begin{aligned} m_1 &= \frac{\text{Upper Arm}}{\text{Forearm \& Hand}} = 1.29 \\ m_2 &= 1 \end{aligned} \quad (3.22)$$

Here, m_2 is defined as $m_2 = 1$ and m_1 is defined accordingly to keep the ratio m_1/m_2 intact, as it is the ratio that affects the movement of the pendulum.

From (Drewniak et al., 2009) we have that the damping coefficient in synovial joints are calculated to be $2.969 \times 10^{-5} \pm 3.409 \times 10^{-5}$ kg m²/s. Hence, we will define ζ as the following.

$$\zeta = 2.969 \times 10^{-5} \quad (3.23)$$

Finally we define g as the earths gravitational acceleration

$$g = 9.81 \quad (3.24)$$

3.6.2 Constraint selection

To be able to minimize the objective function of algorithm (1) we need to define \mathcal{O} , which is the space that constrains λ . Since there is not any straightforward way to find these constraints, we need to define them based on what behavior of the model can be deemed as "acceptable" and what behavior we want to penalize.

The parameters \mathbf{A} and \mathbf{B} explain the magnitude of the forces \mathbf{F} , we do not want these large enough to make either of the pendulums "flip". The upper pendulum flips when it reaches either of the states $\mathbf{x} = [\pm\pi \ \theta_2 \ \omega_1 \ \omega_2]^\top$ and the bottom pendulum flips when reaching either of the states $\mathbf{x} = [\theta_1 \ \pm\pi \ \omega_1 \ \omega_2]^\top$. Several value combination will be tried in order to penalize behaviour sensitive to "flipping" without constraining \mathbf{A} and \mathbf{B} too harshly. Hence \mathbf{A} and \mathbf{B} will be determined from trial and error using a simulation of the model.

The frequency parameters $\mathbf{\Omega}$ are to be decided by the characteristics of the data. $\mathbf{\Omega}$ will be lower bounded by zero and upper bounded by the highest frequency registered by a participant, although with some margins.

The phase shift parameters ϕ are simply constrained by $[0 \ 0] \leq \phi \leq [2\pi \ 2\pi]$ as this contains all the unique phase shifts possible for the forces \mathbf{F} .

3.7 The Van der Pol estimator

In this section we want fit the limit cycle of the van der pol oscillator to the the data described in section 3.3.2, by estimating the parameters of the van der pol limit cycle.

3.7.1 Selection of approximation order

To get started with deriving the Van der Pol estimator, we have to choose which approximation from section 2.1.2 we will use as the function to estimate. Figure 3.10 shows the root mean

square error (RMSE) between approximated limit cycles of the Van der Pol oscillator and their numerical RK4 solutions.

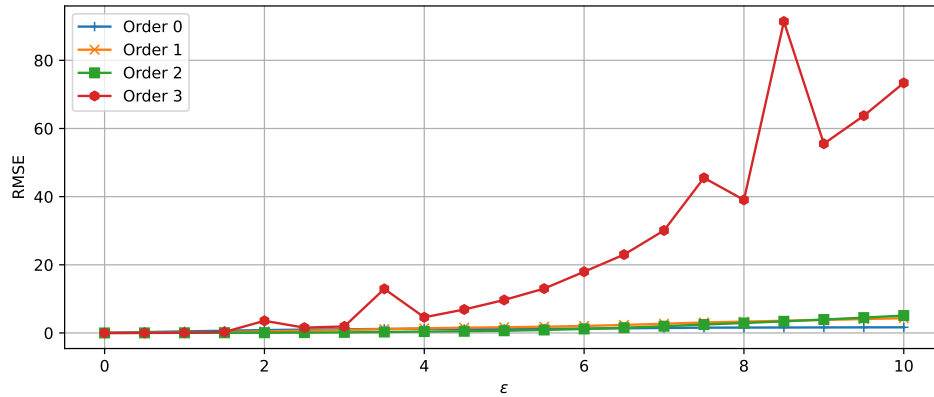
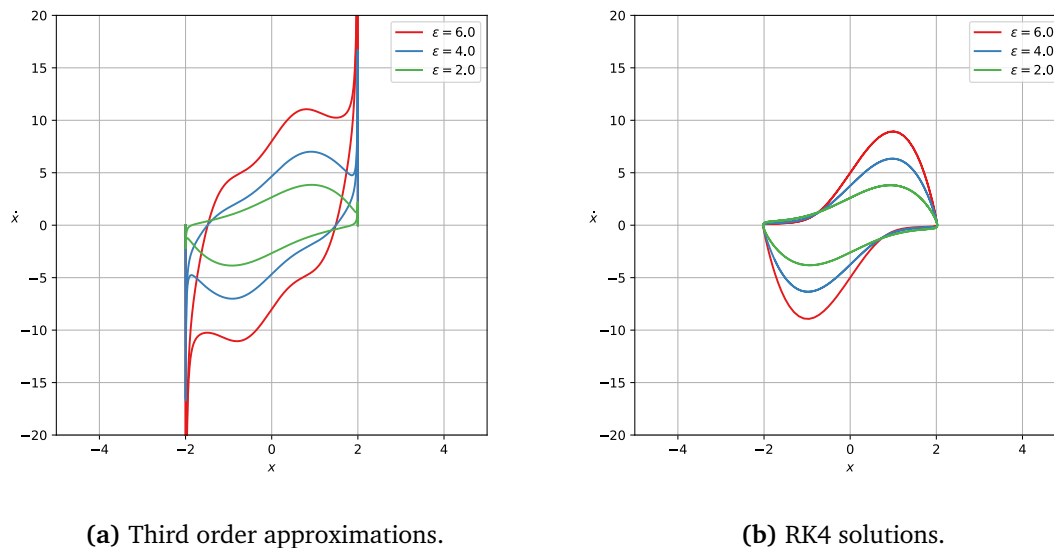


Figure 3.10: RMSE between approximated limit cycles and the RK4 solution.

In figure 3.10 we see that the RMSE for the third-order approximation rises immensely after $\varepsilon \approx 2$ compared to the lower order approximations. The power series approximations are calculated assuming that ε retains values in the neighborhood of $\varepsilon = 0$. However, we also want the estimator to be robust to higher values of ε . Figure 3.11 shows the phase portraits of the limit cycles of the third-order approximation with different values of ε compared to the RK4 solution with the same ε values.



(a) Third order approximations.

(b) RK4 solutions.

Figure 3.11: Phase portraits of the third order approximations and RK4 solutions of the limit cycle.

Both in figure 3.11 and figure 3.10 we clearly see that the third-order approximations are very

sensitive to higher values of ε . Hence we exclude the third-order approximation of the limit cycle as a viable estimator.

Figure 3.12 shows the same RMSE measurements as in figure 3.10 without the third-order approximations.

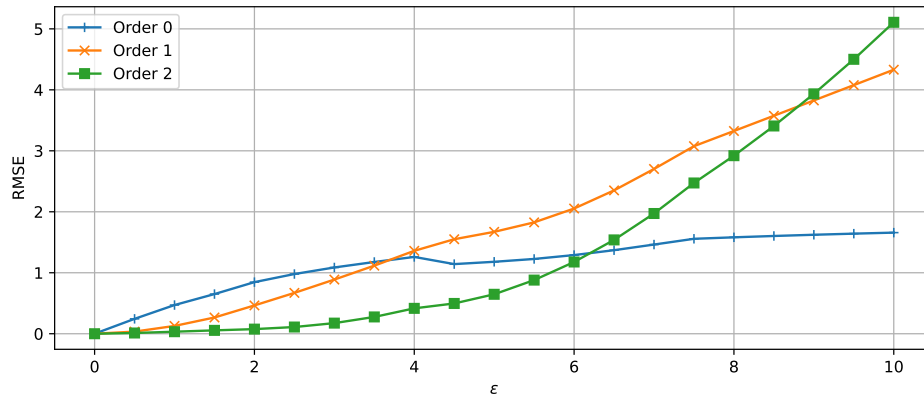
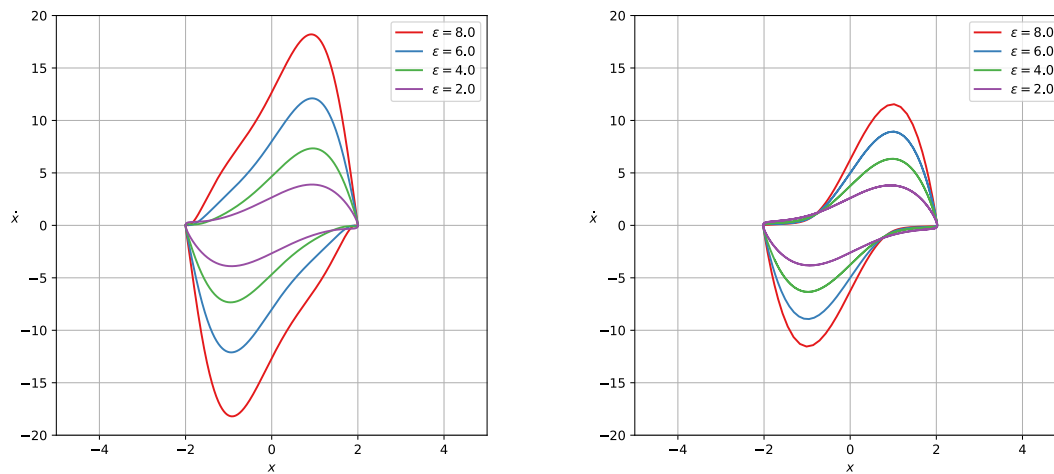


Figure 3.12: RMSE between approximated limit cycles and the RK4 solution.

In figure 3.12 we can see that the second-order retains the highest accuracy until $\varepsilon \approx 6$. For $\varepsilon > 6$, the zeroth-order approximation has the lowest RMSE. Figure 3.13 shows the phase portraits of the limit cycles of the second-order approximation with different values of ε compared to the RK4 solution with the same ε values.



(a) Second order approximations.

(b) RK4 solutions.

Figure 3.13: Phase portraits of the second order approximations and RK4 solutions of the limit cycle.

In figure 3.13, we can see that the second-order approximations are quite robust to higher values of ε . However, when ε is increasing, we see that the second-order approximation becomes increasingly deformed, and the values of \dot{x} get much higher than its RK4 solution counterpart. Since the second-order approximation is undoubtedly the most accurate approximation when $\varepsilon \in [0, 6]$, we choose the second-order approximation of the limit cycle as our estimator, this is done under the assumption that ε will be constrained between $\varepsilon \in [0, 6]$.

3.7.2 Deriving the estimator

Given the data set $(\tilde{x}, \dot{\tilde{x}})^+$ from section 3.3.2 and the second order approximation of the van der pol limit cycle $f_{[2]}^{(+)}$ from section 2.1.2. Treating $\dot{\tilde{x}}$ as the response variable and \tilde{x} as the covariable and $f_{[2]}^{(+)}$ as the regression function, then the least squares estimator, denoted by $\hat{\varepsilon}$ is the value of ε that minimizes

$$\sum_{n=1}^N \left(\dot{\tilde{x}}_n - f_{[2]}^{(+)}(\tilde{x}_n, \varepsilon) \right)^2, \quad \forall \varepsilon \in [0, 6] \quad (3.25)$$

However, there is a few problems with the expression of equation (3.25). Firstly, as seen in figure 3.13a, the *domain* and *codomain* of $f_{[2]}^{(+)}$ can be expressed as, $f_{[2]}^{(+)} : [-2, 2] \times [0, 6] \rightarrow [0, 12]$ i.e when $\varepsilon \in [0, 6]$, \dot{x} , the codomain of $f_{[2]}^{(+)}$ has the upperbound of 12. This is not the case for the response variable $\dot{\tilde{x}}$ which can contain higher values than 12. Hence, we introduce the linear term K , which will scale the function $f_{[2]}^{(+)}$ so its codomain can be increased. Figure 3.14b shows the phase portrait of \tilde{x} , where we can clearly see that $\dot{\tilde{x}}$ contains larger values than the codomain of $f_{[2]}^{(+)}$.

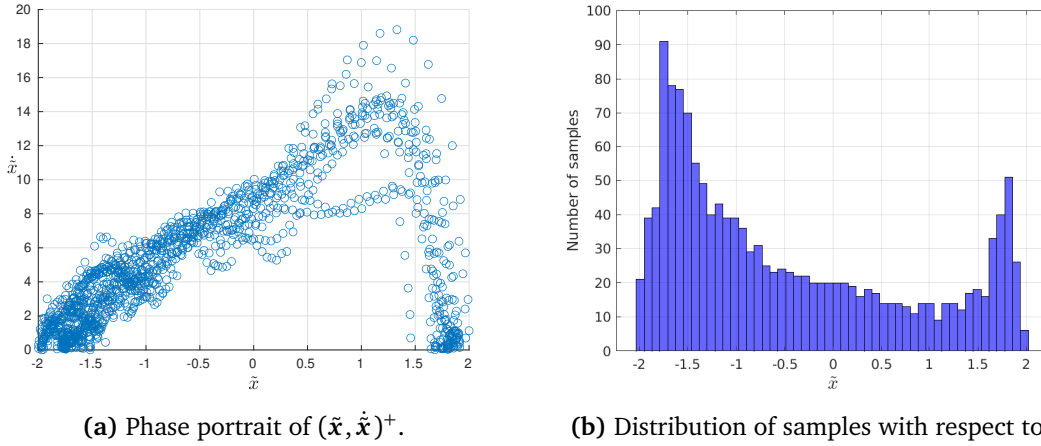


Figure 3.14: Phase portrait and sample distribution from $(\tilde{x}, \dot{\tilde{x}})^+$

In figure 3.14b we see that the distribution of $\dot{\tilde{x}}$ values given evenly spaced intervals of \tilde{x} is not uniform. In practice, this means that intervals of \tilde{x} with a higher density of samples will have a greater influence in estimating $\hat{\varepsilon}$. Hence we introduce the weighting matrix \mathcal{W} to properly

weight each sample with respect to the density of samples nearby. With the new variables K and \mathcal{W} , we can redefine the least-squares estimator as the following optimization problem.

$$\min_{K, \varepsilon} \left\| \mathcal{W}^{\frac{1}{2}} \left(\dot{\tilde{\mathbf{x}}} - K f_{[2]}^{(+)}(\tilde{\mathbf{x}}, \varepsilon) \right) \right\|_2^2 \quad (3.26)$$

Where we define \mathcal{W} as follows.

Let $\tilde{\mathbf{x}}$ be split into M evenly spaced intervals. Then let $\{w\}_{m=1}^M$ denote the number of samples contained in each interval. Finally, we can define the diagonal entries of W as

$$\mathcal{W} = \begin{bmatrix} W_1 & & & \\ & W_2 & & \\ & & \ddots & \\ & & & W_M \end{bmatrix} \quad (3.27)$$

Where $W_m \in \mathbb{R}^{w_m \times w_m}$ is defined as

$$W_m = \begin{bmatrix} \frac{1}{w_m} & & \\ & \ddots & \\ & & \frac{1}{w_m} \end{bmatrix} \quad (3.28)$$

Chapter 4

Results

4.1 Double Pendulum estimator

The optimization problem of algorithm 1 was solved in MATLAB using the Global Optimization Toolbox (MATLAB, R2020b). The numerical solver used for solving the initial value problem in algorithm 1 was a variable-step, variable-order Adams-Moulton predictor-corrector solver implemented as "ode113" in MATLAB (Shampine and Reichelt, 1997). This solver was preferred over the classical ode solver "ode45", as systems that exhibit chaotic behaviour requires more precise solvers (Chen, 2008).

The parameters of λ were estimated for all the interval stages across all test days for every participant.

4.1.1 Estimator Performance

The double pendulum model was simulated with the estimated parameters λ for all participants (from a specific stage on a specific incline test day). The FIT and MSE errors between $\hat{\theta}_e$ and θ_e and between $\hat{\theta}_h$ and θ_h were fit to a gaussian distribution using maximum likelihood estimation. Table 4.1 and 4.2 show the mean and standard deviation for the FIT and MSE distributions, where μ denotes the mean and σ denotes the standard deviation.

Elbow		Hand		Stage	Incline
μ	σ	μ	σ		
5.00	34.58	-143.59	116.98	1	0.5%
-13.65	32.49	-120.02	105.37	2	
-18.95	29.23	-81.89	60.59	3	
-4.25	36.85	-270.32	190.43	1	2.5%
-9.92	30.08	-151.69	114.36	2	
-7.08	24.92	-102.12	74.30	3	
19.43	35.62	-350.31	235.23	1	5.0%
-26.24	113.36	-1530.07	5818.87	2	
-16.58	28.71	-90.39	48.54	3	

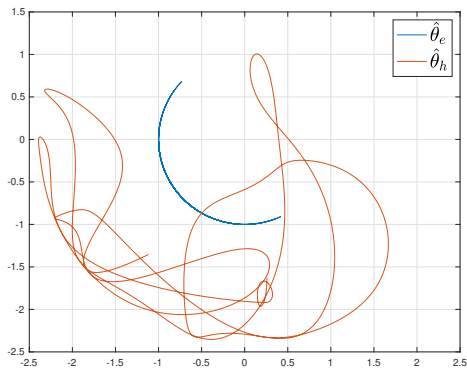
Table 4.1: Double pendulum FIT distributions.

Elbow		Hand		Stage	Incline
μ	σ	μ	σ		
0.15	0.05	0.07	0.04	1	0.5%
0.20	0.08	0.10	0.06	2	
0.21	0.10	0.11	0.08	3	
0.15	0.07	0.06	0.03	1	2.5%
0.16	0.07	0.07	0.04	2	
0.15	0.05	0.08	0.07	3	
0.09	0.04	0.06	0.05	1	5.0%
0.17	0.19	0.14	0.39	2	
0.13	0.05	0.04	0.02	3	

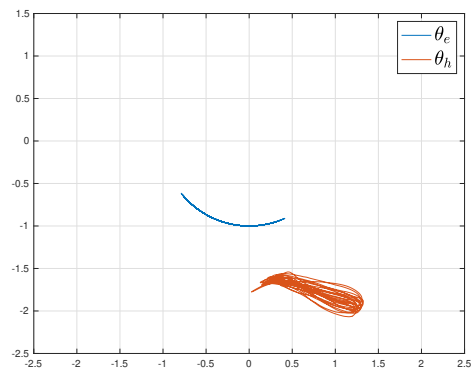
Table 4.2: Double pendulum MSE distributions.

The FIT and MSE values clearly show that the model does not fit the observed values well. Negative FIT values convey that the model fits the data worse than the mean values of the data. This signifies that our model does not explain the essence of data.

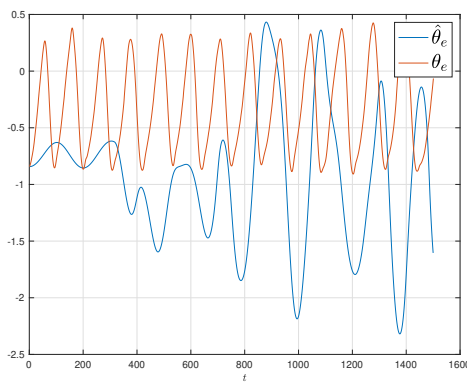
In figures 4.1, 4.2 and 4.3 we can see the observed values θ_e and θ_h plotted against the estimated values $\hat{\theta}_e$ and $\hat{\theta}_h$.



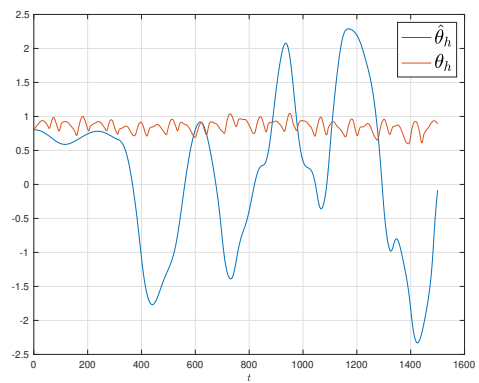
(a) Cartesian positions of $\hat{\theta}_e$ and $\hat{\theta}_h$



(b) Cartesian positions of θ_e and θ_h



(c) $\hat{\theta}_e$ and θ_e with FIT = -484.6



(d) $\hat{\theta}_h$ and θ_h with FIT = -26208.7

Figure 4.1: The worst performance of the simulated model with estimated parameters.

Figure 4.1 shows the estimation with the worst performance. Here we can clearly see that the estimated values of λ did not produce stable oscillations, and the estimated values of $\hat{\theta}_e$ and $\hat{\theta}_h$ behave somewhat chaotic.

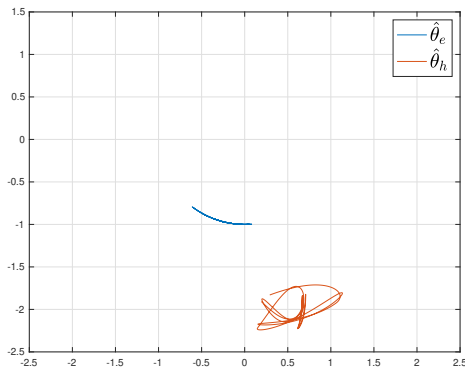
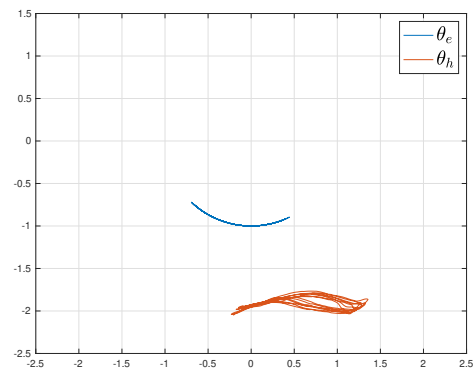
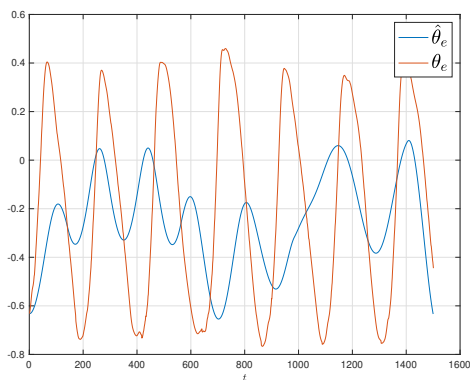
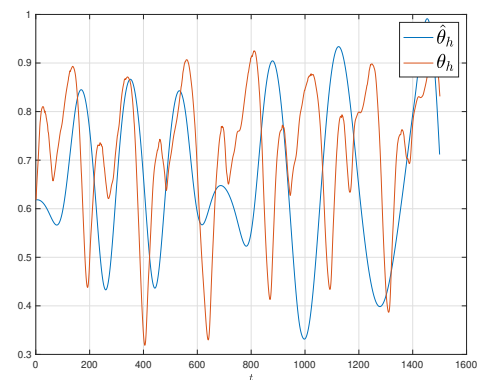
(a) Cartesian positions of $\hat{\theta}_e$ and $\hat{\theta}_h$ (b) Cartesian positions of θ_e and θ_h (c) $\hat{\theta}_e$ and θ_e with FIT = -15.1(d) $\hat{\theta}_h$ and θ_h with FIT = -137.4**Figure 4.2:** Average performance of the simulated model with estimated parameters.

Figure 4.2 shows an estimation of $\hat{\theta}_e$ and $\hat{\theta}_h$ with average performance. We can observe in figure 4.2a that the estimated values of $\hat{\theta}_e$ and $\hat{\theta}_h$ do oscillate in the same region as the observed values in figure 4.2b. However, we can see that its shape does not transfer well to the observed values. Figure 4.2c and 4.2d also show that both phase and values of $\hat{\theta}_e$ and $\hat{\theta}_h$ are quite different from the observed data.

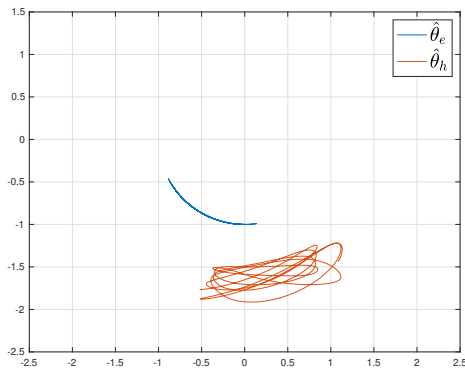
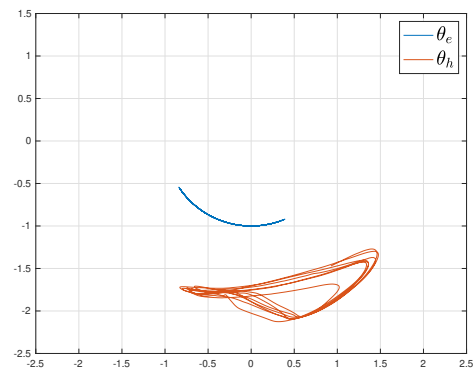
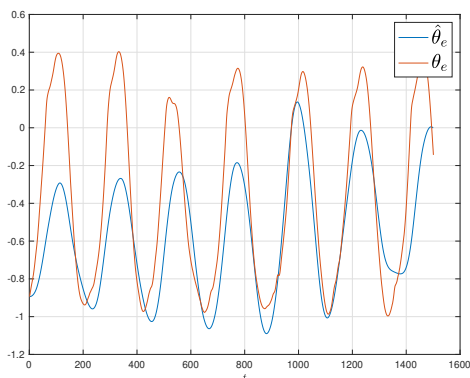
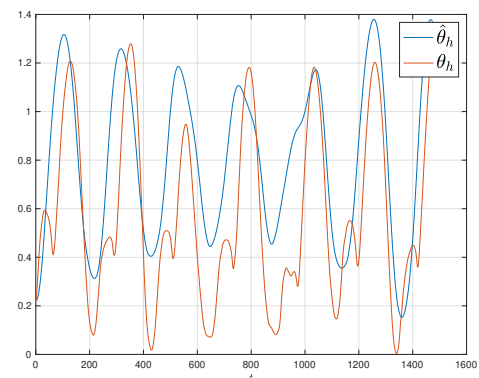
(a) Cartesian positions of $\hat{\theta}_e$ and $\hat{\theta}_h$ (b) Cartesian positions of θ_e and θ_h (c) $\hat{\theta}_e$ and θ_e with FIT = 50.4(d) $\hat{\theta}_h$ and θ_h with FIT = 21.4**Figure 4.3:** The best performance of simulated model with estimated parameters.

Figure 4.2 shows the estimation of $\hat{\theta}_e$ and $\hat{\theta}_h$ with the best performance. We can observe in figure 4.3a that the estimated values of $\hat{\theta}_e$ and $\hat{\theta}_h$ do oscillate in the same region as the observed values in figure 4.3b and share somewhat similar shape. Furthermore, we can see figure 4.3c and 4.3d that the difference in phase from the estimated and observed values are quite small and values of $\hat{\theta}_e$ and $\hat{\theta}_h$ are quite different from the observed data.

4.1.2 Heart Rate and Energy Expenditure Correlation

To examine if there is any correlation between the estimated parameters λ and the heart rate and energy expenditure centroids, we perform PCA on λ for every experiment and substage. We do this with the hopes of gathering the variance explained by λ in fewer dimensions.

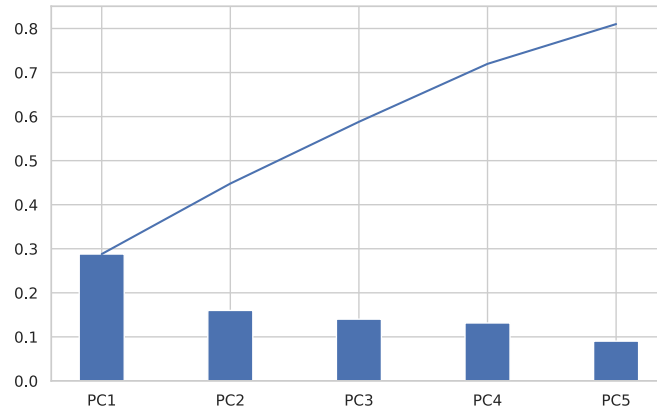


Figure 4.4: Explained variance from each principal component with plot of cumulative explained variance.

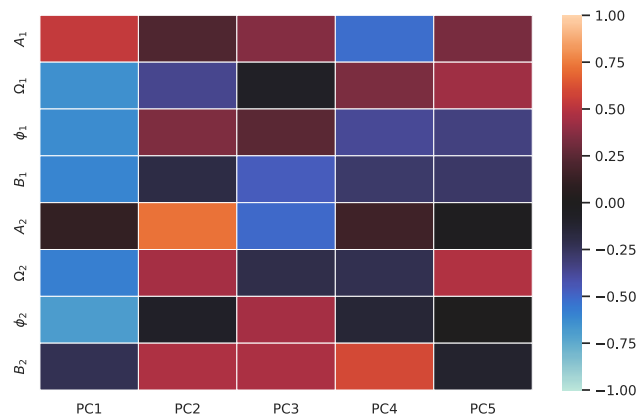
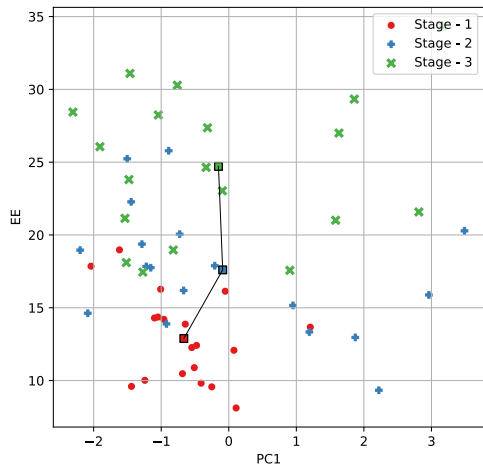


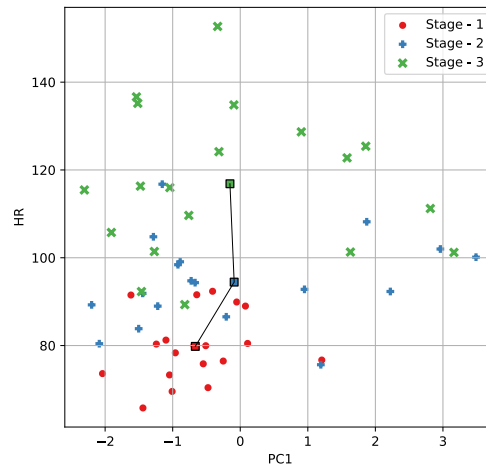
Figure 4.5: Correlation loadings heatmap between the parameters of λ and the principal components.

Figure 4.4 shows the explained variance from each principal component and figure 4.5 show what parameters of λ contributes to which of the principal components. In figure 4.5 we can see that the first two principal components are explained well by all the parameters of λ . This also provides the information that many of the parameters of λ are correlated to each other. Hence we proceed with using the first two principal components for further analysis.

Figures 4.6 and A.5 shows the two first principal components plotted against the energy expenditure and heart rate centroids for all participants and interval stages during the 0.5% incline test day.

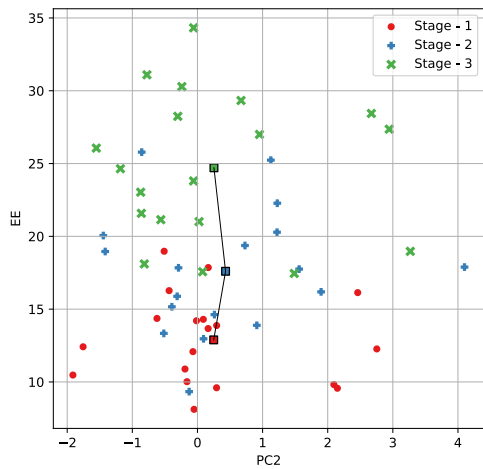


(a) PC1 plotted against EE.

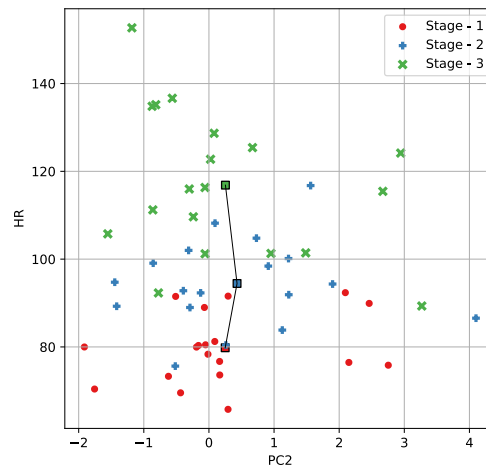


(b) PC1 plotted against HR.

Figure 4.6: Scatter plot from the 0.5% incline test day of the first principal component against energy expenditure and heart rate. The center of the clusters from each stage are marked as squares.



(a) PC2 plotted against EE.



(b) PC2 plotted against HR.

Figure 4.7: Scatter plot from the 0.5% incline test day of the second principal component against energy expenditure and heart rate. The center of the clusters from each stage are marked as squares.

It is quite clear from the plots of figures 4.6 and A.5 that there is no clear clustering of the values of the principal components. The values of the first and second principal component during the different stages seems to be somewhat randomly distributed. Neither is there any

visible correlation between the principal components and heart rate or energy expenditure.

Since the precision of the model is measured to be very inaccurate, the double pendulum will not be used to perform any further analysis. The plots equivalent to figures 4.6 and A.5 for the 2.5% and 5.0% test days are provided in the appendix, A.3.

4.2 Van der pol estimator

The nonlinear optimization problem of equation (3.26) was solved in MATLAB using the Global Optimization Toolbox (MATLAB, R2020b). The parameters K and ε were estimated for all the interval stages across all test days for every participant.

4.2.1 Estimator Performance

The FIT and MSE errors between $\dot{\hat{x}}^{(+)}$ and $\hat{K}f_{[2]}^{(+)}(\tilde{\mathbf{x}}, \hat{\varepsilon})$ was calculated for all participants (from a specific stage on a specific incline test day), and fit to a gaussian distribution using maximum likelihood estimation. Table 4.3 and 4.4 show the mean and standard deviation for the MSE and FIT distributions, where μ denotes the mean and σ denotes the standard deviation.

Elbow		Hand		Stage	Incline
μ	σ	μ	σ		
57.42	27.16	54.71	17.91	1	0.5%
44.56	29.55	47.12	23.70	2	
35.35	29.70	36.03	21.92	3	
59.23	27.12	46.12	19.83	1	2.5%
46.05	28.70	37.56	22.89	2	
46.19	32.73	36.11	24.76	3	
65.44	17.49	57.34	18.26	1	5.0%
56.70	17.32	39.51	22.67	2	
44.14	28.57	32.97	21.18	3	

Table 4.3: Van der pol estimator FIT distributions.

Elbow		Hand		Stage	Incline
μ	σ	μ	σ		
7.77	8.06	7.67	4.76	1	0.5%
15.92	11.10	15.43	9.63	2	
24.20	10.48	25.46	12.22	3	
5.32	5.52	6.65	4.87	1	2.5%
9.13	7.76	10.28	6.77	2	
11.97	9.40	13.88	7.28	3	
2.72	2.24	3.33	2.54	1	5.0%
5.50	4.75	7.81	6.61	2	
10.21	8.55	12.66	8.13	3	

Table 4.4: Van der pol estimator MSE distributions.

From a first look at the error distributions in table 4.3 and 4.4, we can see that the overall performance is quite good in comparison to the double pendulum estimator. This is a good indicator that the arm movement exhibits some similar behavior to the Van der Pol limit cycle.

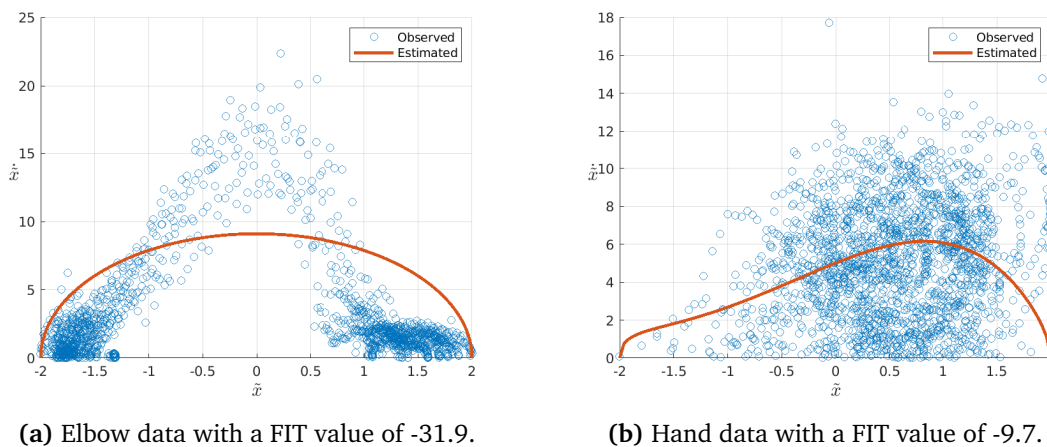


Figure 4.8: The observed values from $(\tilde{x}, \dot{\tilde{x}})^+$ plotted with the estimated values from $\hat{K}f_{[2]}^{(+)}(\tilde{x}, \hat{\varepsilon})$ with the worst FIT values.

Figure 4.8 shows the cases where the van der pol estimator performed the worst for the elbow and hand-tracked data. For the elbow data, it is clear that the speed distribution during the elbow movement is not similar to the van der pol limit cycle. For the hand data, the speed distribution is clearly non-consistent for each cycle the data represents and consequently fits poorly with the van der pol estimator.

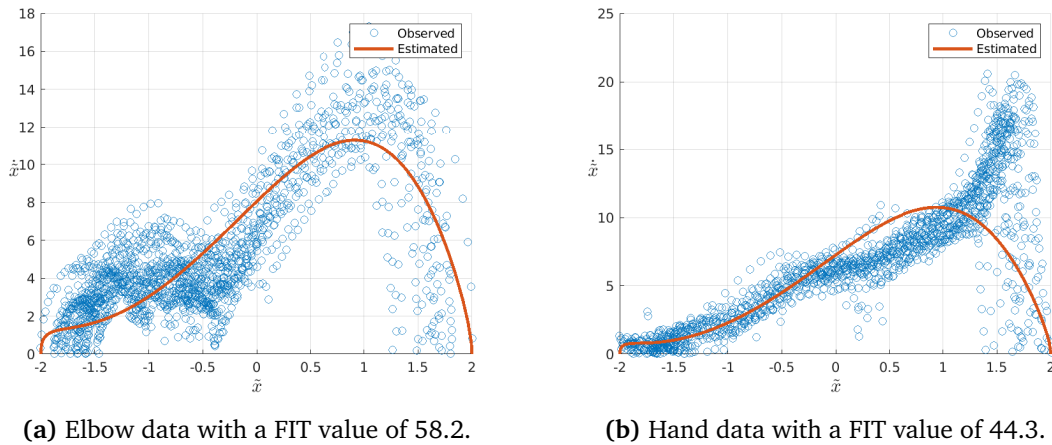


Figure 4.9: The observed values from $(\tilde{\mathbf{x}}, \dot{\tilde{\mathbf{x}}})^+$ plotted with the estimated values from $\hat{K}f_{[2]}^{(+)}(\tilde{\mathbf{x}}, \hat{\varepsilon})$ with average FIT values.

Figure 4.9 shows how the average-case performance of the estimator looks for the elbow and hand-tracked data. The shapes of the distributions in both figure 4.9a and figure 4.9a share similarities with the van der pol limit cycle. For the elbow data, the speed distribution is slightly inconsistent for each movement cycle, hence the high variance in the $\dot{\tilde{\mathbf{x}}}$ direction. For the hand data, the speed distribution is a little skewed to the right, yielding a somewhat imprecise fit to the van der pol estimator.

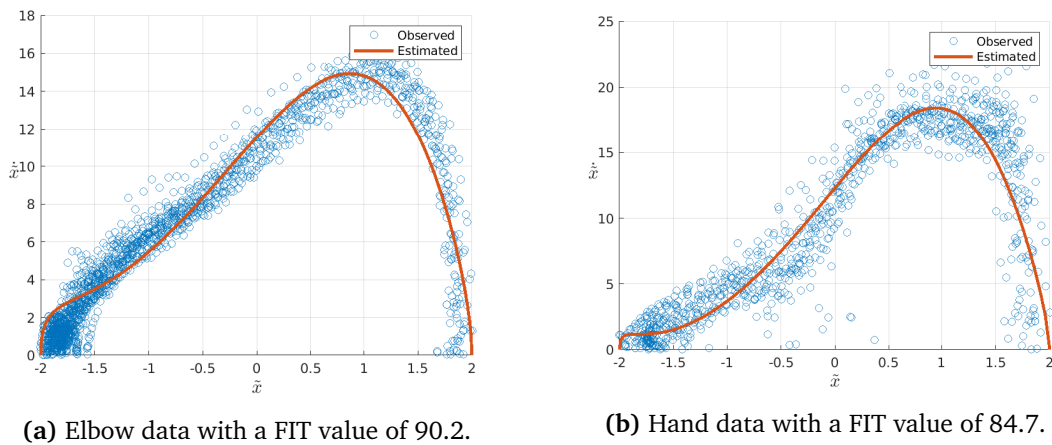


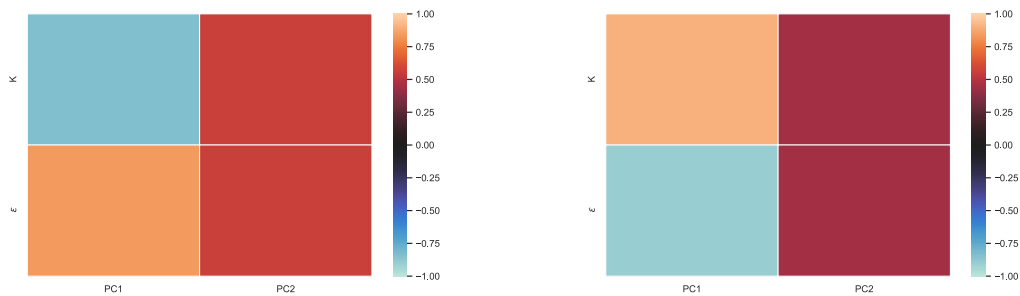
Figure 4.10: The observed values from $(\tilde{\mathbf{x}}, \dot{\tilde{\mathbf{x}}})^+$ plotted with the estimated values from $\hat{K}f_{[2]}^{(+)}(\tilde{\mathbf{x}}, \hat{\varepsilon})$ with the best FIT values.

Figure 4.8 shows the cases where the van der pol estimator performed the best for the elbow and hand-tracked data. Both fit the model very well, although there is a little more variance in the $\dot{\tilde{\mathbf{x}}}$ direction for the hand data.

4.2.2 Correlations with heart rate and energy expenditure

The estimated values K and ε are reduced to one variable using PCA. This is done because we believe the relationship between the two variables is important. Hence, by using PCA, we can find the linear combination of K and ε that explains the most variance in the space created by K and ε .

Figure 4.11 shows the correlation loadings of the PCA performed on the elbow and hand data. The heatmap indicates how much a variable contributes to a principal component. Furthermore, in figure 4.11a and figure 4.11b, we can see that K and ε both contribute a lot to the first principal component, signifying that both parameters have high explanatory power.



(a) Correlation loadings for the elbow data.

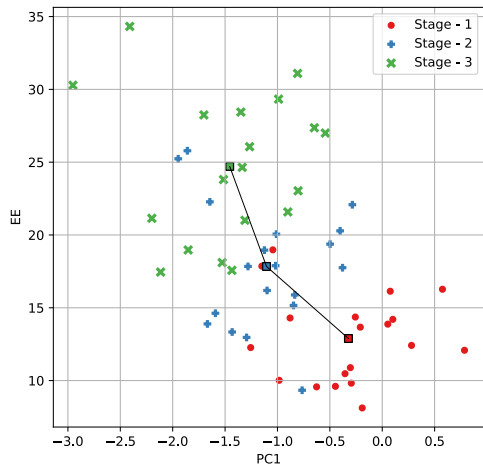
(b) Correlation loadings for the hand data.

Figure 4.11: The correlation loadings shows the correlation between the estimated values of K and ε and the principal components.

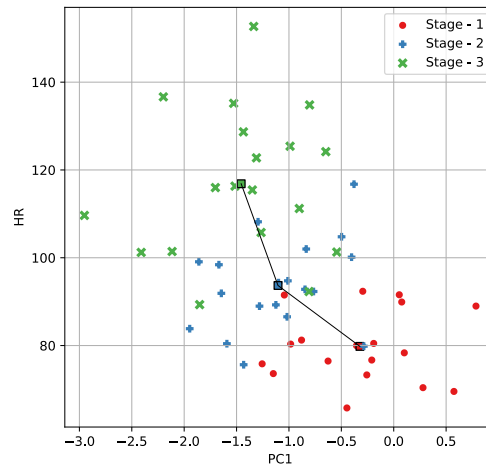
The explained variance by the first principle component from the elbow data and hand data are 68% and 80%, respectively.

Elbow data

Figures 4.12, 4.13 and 4.14 show the first principal component of K and ε from the elbow data plotted against the energy expenditure and heart rate centroids for all participants and interval stages during the 0.5%, 2.5% and 5.0% incline test days.

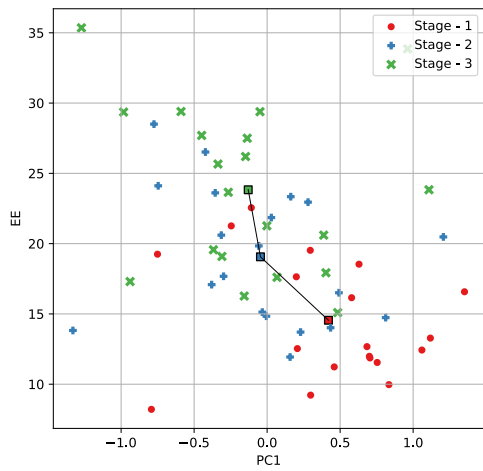


(a) PC1 plotted against EE.

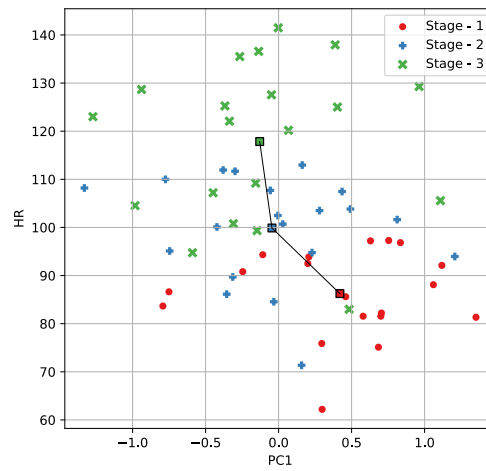


(b) PC1 plotted against HR.

Figure 4.12: Scatter plot from the 0.5% incline test day of the first principal component against energy expenditure and heart rate. The center of the clusters from each stage are marked as squares.



(a) PC1 plotted against EE.



(b) PC1 plotted against HR.

Figure 4.13: Scatter plot from the 2.5% incline test day of the first principal component against energy expenditure and heart rate. The center of the clusters from each stage are marked as squares.

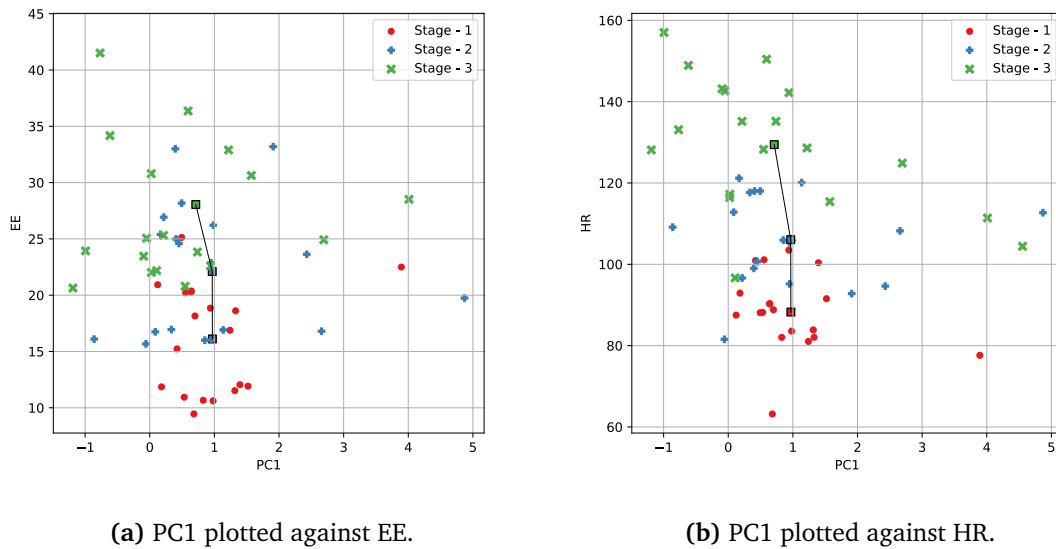


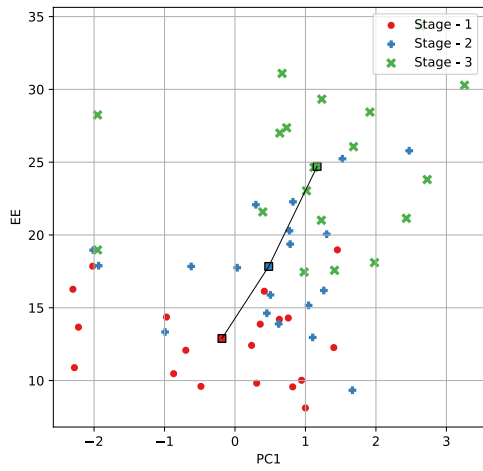
Figure 4.14: Scatter plot from the 5.0% incline test day of the first principal component against energy expenditure and heart rate. The center of the clusters from each stage are marked as squares.

Figure 4.12 depicts the first principal component of K and ε plotted against HR and EE. We can observe that there is a formation of clusters at each stage. There is also a visible correlation between PC1 and HR or EE. Clearly, a decreasing value in the first principal component indicates an increase in energy expenditure and heart rate. However, in figures 4.13 and 4.14 we observe that when the incline rises, the relations between PC1, EE and HR becomes more vague and the clusters less dense.

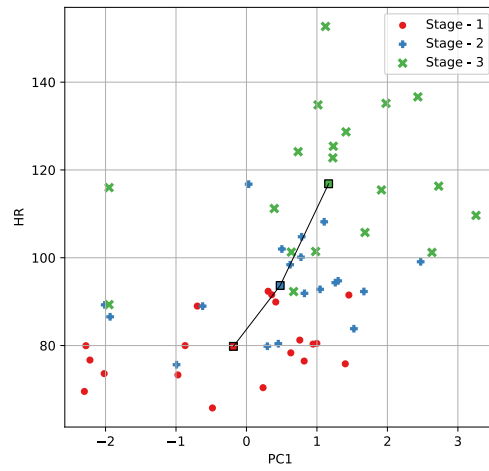
Generally, we can see a high variance between participants in the PC1 direction within each stage through all incline test days and a significant increase in variance as the incline increases.

Hand data

Figures 4.15, 4.16 and 4.17 show the first principal component of K and ε from the hand data plotted against the energy expenditure and heart rate centroids for all participants and interval stages during the 0.5%, 2.5% and 5.0% incline test days.

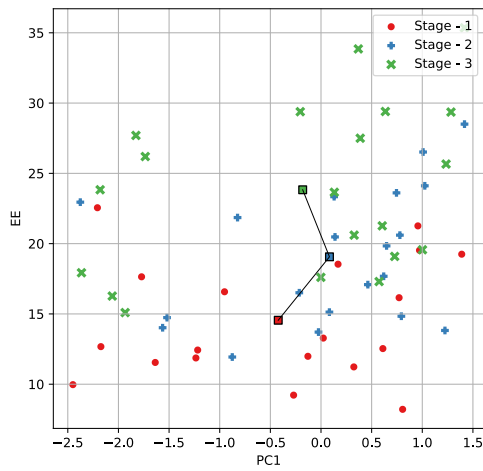


(a) PC1 plotted against EE.

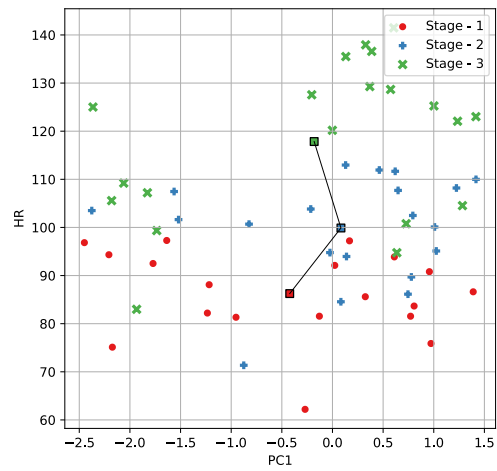


(b) PC1 plotted against HR.

Figure 4.15: Scatter plot from the 0.5% incline test day of the first principal component against energy expenditure and heart rate. The center of the clusters from each stage are marked as squares.



(a) PC1 plotted against EE.



(b) PC1 plotted against HR.

Figure 4.16: Scatter plot from the 2.5% incline test day of the first principal component against energy expenditure and heart rate. The center of the clusters from each stage are marked as squares.

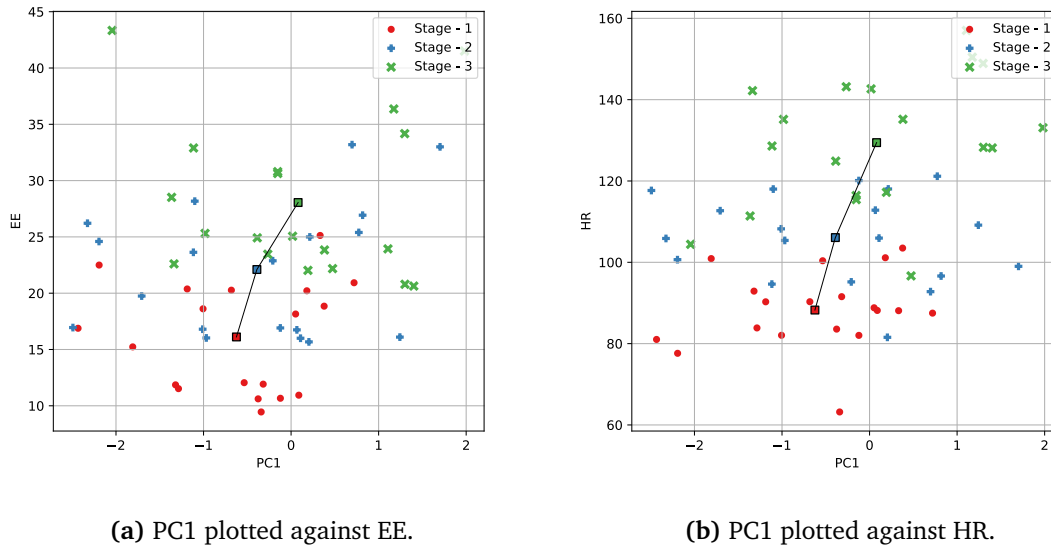


Figure 4.17: Scatter plot from the 5.0% incline test day of the first principal component against energy expenditure and heart rate. The center of the clusters from each stage are marked as squares.

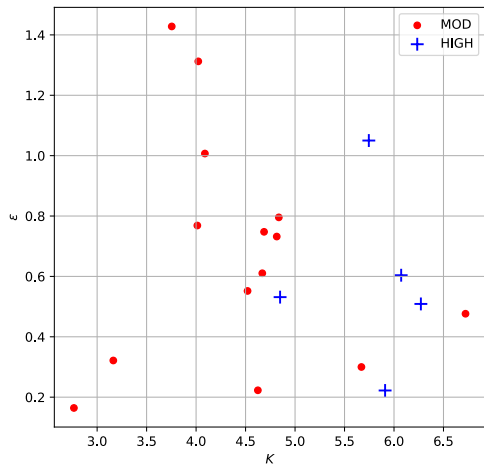
Figure 4.15 depicts the first principal component of K and ε plotted against HR and EE. We can observe that there is a formation of clusters at each interval stage. There also seems to be a weak correlation between PC1 and HR or EE. However, it is generally a very high variance of PC1 values within each interval stage.

For the 2.5 and 5.0% test days, depicted in figure 4.16 and figure 4.17, there is not much information to be found at all as the PC1 values seem to be somewhat scattered randomly.

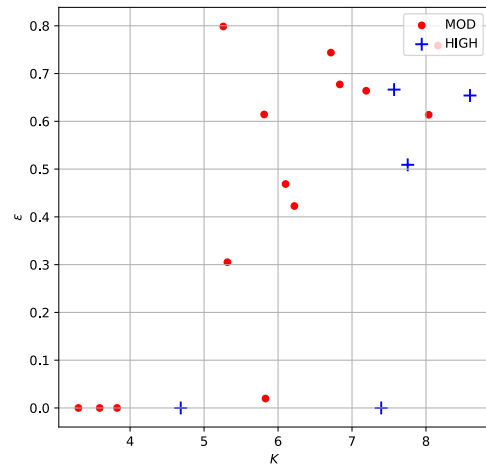
4.2.3 IPAQ and Gender correlation

IPAQ and Gender are two of the demographic variables we suspect may share correlations with the estimated parameters from the Van der Pol estimator. IPAQ levels, described in section 1.2.2, indicate how physically active a participant is. Of the 20 participants, 5 participants score high on the IPAQ test, and the remainder of the participants score moderate. From table 1.1, we can see the different thread mill speeds of the interval stages. The interval stages for men are 1 km/h higher than for women; hence we expect to see overall higher K and ε values for men than women.

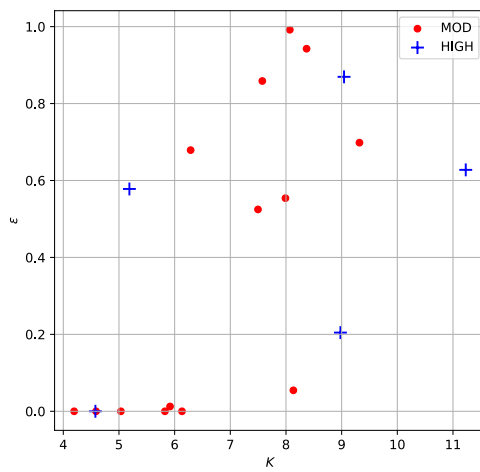
Furthermore, in this section, we want to investigate if there is some connection between the parameters K and ε and the variables IPAQ and Gender.



(a) K plotted against ε from interval stage 1.

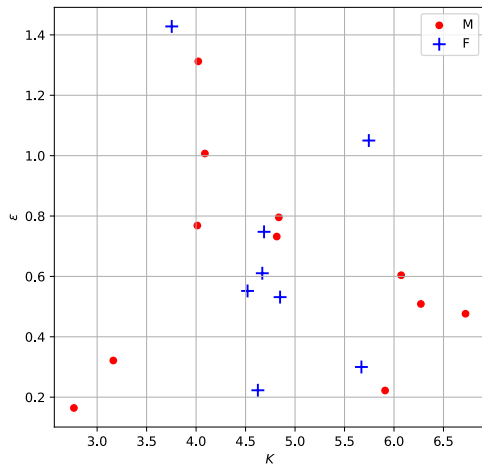


(b) K plotted against ε from interval stage 2.

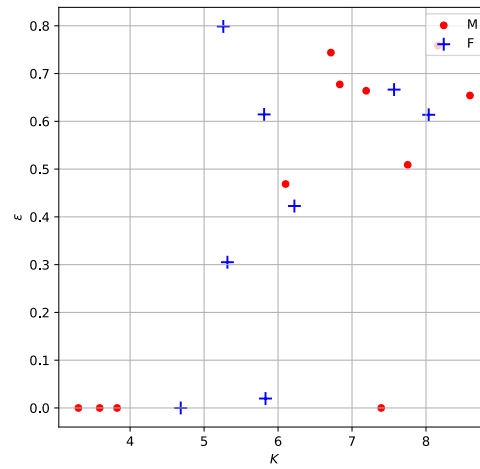


(c) K plotted against ε from interval stage 3.

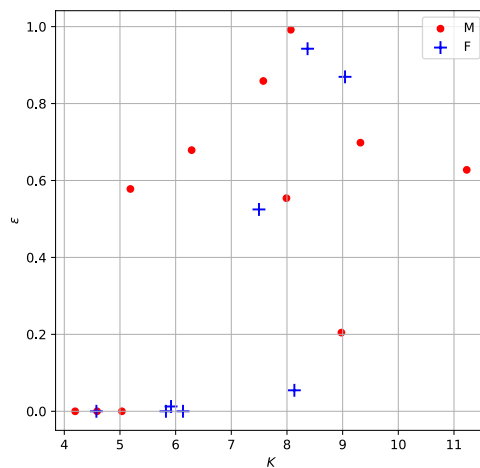
Figure 4.18: K and ε from the elbow data for all participants during the 0.5% test day with IPAQ levels marked as HIGH or MOD (moderate).



(a) K plotted against ε from interval stage 1.



(b) K plotted against ε from interval stage 2.



(c) K plotted against ε from interval stage 3.

Figure 4.19: K and ε from the elbow data for all participants during the 0.5% test day with gender marked as M for male and F for female.

Figures 4.18 and 4.19 show the estimated values of K and ε from elbow data during the 0.5% test day with marked IPAQ and gender values. In figure 4.19a we can see that participants with HIGH IPAQ generate higher K values. Apart from this, there is not much information to be found in the other interval stages and test days. The plots from the other 2.5% and 5.0% incline test days are provided in the appendix A.3.2.

The same holds for the plots in figure 4.19 where there is also no clear connection between K , ε , and gender, even though men roll at higher speeds than women.

Chapter 5

Discussion

5.1 Model performances

5.1.1 The double pendulum estimator

To make a simplified mathematical model of the human arm, we went towards a design using the double pendulum. Our goal was to express the forces acting upon the pendulum as signals with unknown parameters to be decided from least-squares estimation. The least-squares estimation, which was solved with a derivative-free optimization method, produced poor results. There may be numerous reasons why the performance of the model is so inaccurate.

Firstly the characteristics of the human arm and the forces it can produce are very complex. The one-dimensional forces we modeled were a considerable simplification of these. To be able to keep the number of unknown parameters down, we only modeled the forces in one dimension. These simplifications were also done to make the optimization problem computationally feasible, as an increase in parameters vastly increased the computational complexity of the optimization problem. Sacrificing a dimension of the forces acting on the pendulum may have had a large impact on the precision of the model.

Secondly, the double pendulum is a dynamical system that exhibits chaotic behavior (Shinbrot et al., 1992). Meaning that the system is very sensitive to initial conditions and inputs. As the system is so sensitive to small changes, the choice of numerical solver is very important. This is shown in (Chen, 2008), where the two MATLAB solvers used, *ode45* and *ode113*, were used to simulate the double pendulum and produced very different results. Furthermore, from (T. Stachowiak and Okada, 2006) it is shown how amounts of energy in the double pendulum system increases the chaotic behavior, and makes the system stray more from quasi-periodic behavior. This might be relevant to our model as we increase total energy by introducing external forces. The system's high energy could make it more difficult for the estimator to find quasi-periodic orbits similar to what we see in the data and possibly, as shown in figure 4.1, not find any quasi-periodic orbits at all.

5.1.2 The van der pol estimator

The van der pol oscillator described in section 2.1 was approached from an analytical perspective, where we approximated its limit cycle as a continuous function. We expected to see some similar behavior between the phase portraits of the arm movements and the limit cycle itself. This was done with relatively high precision with the help of a scaling parameter K . Although the introduction of K made the model precise, it made the results harder to interpret. PCA was put to use to find the best linear combination of the estimated parameters; however, it is hard to say whether this linear combination acceptably represented all estimations.

One problem with the estimator was participants who reached their speed climax earlier in their movement cycle. These cases were hard to explain with the model and made unreliable parameter estimations. In figure 4.8a, we see an example of this.

5.2 Correlations with heart rate and energy expenditure

Generally, there was shown little correlation between heart rate and energy expenditure from the estimated variables.

The parameters from the double pendulum estimator showed no potential in explaining the participants' heart rate and energy expenditure. Furthermore, it was so imprecise that any found correlations would have been deemed untrustworthy.

The parameters estimated from the van der pol estimator, on the other hand, showed higher potential as indicators of energy expenditure and heart rate. As shown in section 4.2.2, on the 0.5% test day, there was visible clustering amongst the interval stages and correlations between heart rate and energy expenditure. However, as the incline was increased, the estimated parameters showed little potential as the clustering worsened and the variance increased.

5.3 Correlations with demographic variables

We examined the relationship between the estimated parameters K and ε and the demographic variables IPAQ and Gender without finding any clear connections. It would have been interesting to see if there was a connection between people living more physically active lifestyles and their movement characteristics; however, this was not our observation. Furthermore, there were neither found any connections between K and ε and gender. This was somewhat a surprise as men rolled at higher speeds than women, although the difference in speed might have been too small to be recognized from the estimated parameters.

5.4 Model Generalizability

Of the 20 participants in the study, there were seen lots of different shaped trajectories of arm movement. In figures 4.1, 4.2 and 4.3 we see three cases with very different movement. The participants show unique styles of movement, and this does pose a challenge when we have the goal of parameterizing their movement.

Of the two models, the double pendulum is the model with the best potential to fit the unique

movement of the participants. As it can theoretically, with the right external forces, fit any movement the arm can do. However, with this versatility, problems in terms of model and computational complexity arise.

The van der pol model, on the other hand, did fit the data quite well. However, when people with unique movements or speed patterns do not fit the van der pol limit cycle shape, there is a guaranteed mismatch between the model and the data.

5.5 Further Research

A central future objective is to increase the model performances. Regarding the double pendulum, more mathematical modeling could prove useful. Constraining the model in likeness to the human arm and making a more sophisticated model of friction are two things that were not implemented due to a shortage of available time.

Of all 33 motion tracked points on the body and wheelchair, we only made use of 3 of them. More advanced models could make use of even more trajectories to extract more information from the experiments.

Through the results and discussion, we have seen that when the incline increases, the van der pol estimator performance decreases, and the correlations between heart rate and energy expenditure vanish. By using different preprocessing methods for the data, the increase in incline could have been accounted for, and the results could have possibly been improved.

Chapter 6

Concluding remarks

In this study, we tried to explain the motion-captured trajectories of wheelchair users as mathematical models. The double pendulum model did show the potential of working as a general model for the human arm but did not provide any useful information related to energy expenditure or heart rate, possibly due to its low precision. Although, more precise modeling and a different approach to the optimization problem could increase the performance of the model

Correlation between the parameters estimated from the Van der Pol estimator and heart rate and energy expenditure were observed on the 0.5% test day. This suggests that there is a possibility to connect arm movement characteristics to heart rate and or energy expenditure.

No significant connections were found between the demographic variables and the estimated parameters from the van der pol estimator. If there is a connection between arm movement characteristics, IPAQ, or gender, the Van der Pol estimator was not able to explain it.

Further research should be conducted towards finding better models for motion-captured trajectories, which may lead to more significant and interesting results.

Bibliography

- Abdi, Hervé and Lynne J Williams (2010). 'Principal component analysis'. In: *Wiley interdisciplinary reviews: computational statistics* 2.4, pp. 433–459.
- Agarana, Michael C and Esther T Akinlabi (2018). 'Mathematical Modelling and Analysis of Human Arm as a Triple Pendulum System using Euler–Lagrangian Model'. In: *IOP Conference Series: Materials Science and Engineering*. Vol. 413. 1. IOP Publishing, p. 012010.
- Bieda, Robert and Krzysztof Jaskot (2018). 'The Mathematical Model of the Human Arm'. In: *Advanced Technologies in Practical Applications for National Security*. Springer, pp. 241–266.
- Bogdanov, Alexander (2004). 'Optimal control of a double inverted pendulum on a cart'. In: *Oregon Health and Science University, Tech. Rep. CSE-04-006, OGI School of Science and Engineering, Beaverton, OR*.
- Brockway, JM (1987). 'Derivation of formulae used to calculate energy expenditure in man.' In: *Human nutrition. Clinical nutrition* 41.6, pp. 463–471.
- Butcher, John Charles (2016a). *Numerical methods for ordinary differential equations*. John Wiley & Sons, pp. 93–113.
- Butcher, John Charles (2016b). *Numerical methods for ordinary differential equations*. John Wiley & Sons, pp. 105–113.
- Chen, Joe (2008). 'Chaos from simplicity: an introduction to the double pendulum'. In.
- Craig, Cora L, Alison L Marshall, Michael Sjöström, Adrian E Bauman, Michael L Booth, Barbara E Ainsworth, Michael Pratt, ULF Ekelund, Agneta Yngve, James F Sallis et al. (2003). 'International physical activity questionnaire: 12-country reliability and validity.' In: *Medicine and science in sports and exercise* 35.8, pp. 1381–1395.
- Drewniak, Elizabeth I, Gregory D Jay, Braden C Fleming and Joseph J Crisco (2009). 'Comparison of two methods for calculating the frictional properties of articular cartilage using a simple pendulum and intact mouse knee joints'. In: *Journal of biomechanics* 42.12, pp. 1996–1999.
- Fagard, Robert H and Véronique A Cornelissen (2007). 'Effect of exercise on blood pressure control in hypertensive patients'. In: *European Journal of Preventive Cardiology* 14.1, pp. 12–17.
- FitzHugh, Richard (1961). 'Impulses and physiological states in theoretical models of nerve membrane'. In: *Biophysical journal* 1.6, pp. 445–466.
- French, Dustin D, Robert R Campbell, Sunil Sabharwal, Audrey L Nelson, Polly A Palacios and Deborah Gavin-Dreschnack (2007). 'Health care costs for patients with chronic spinal cord injury in the Veterans Health Administration'. In: *The journal of spinal cord medicine* 30.5, pp. 477–481.
- Gros, Sebastien (2021). 'Lecture notes, TTK4130 - Modelling and Simulation'. In.

- Kipp, Shalaya, William C Byrnes and Rodger Kram (2018). 'Calculating metabolic energy expenditure across a wide range of exercise intensities: the equation matters'. In: *Applied Physiology, Nutrition, and Metabolism* 43.6, pp. 639–642.
- Kirshblum, Steven C, William Waring, Fin Biering-Sorensen, Stephen P Burns, Mark Johansen, Mary Schmidt-Read, William Donovan, Daniel E Graves, Amitabh Jha, Linda Jones et al. (2011). 'Reference for the 2011 revision of the international standards for neurological classification of spinal cord injury'. In: *The journal of spinal cord medicine* 34.6, pp. 547–554.
- MATLAB (R2020b). *MATLAB Optimization Toolbox*. The MathWorks, Natick, MA, USA.
- Metamax (n.d.). *Vyntus CPX/portable Metamax II*. URL: https://www.ntnu.edu/documents/221360533/221362168/MMX+II_050419_e+%282%29.pdf/e86c0c4f-6cbf-4c1e-937b-301a0b008a9c.
- Nagumo, Jinichi, Suguru Arimoto and Shuji Yoshizawa (1962). 'An active pulse transmission line simulating nerve axon'. In: *Proceedings of the IRE* 50.10, pp. 2061–2070.
- Nocon, Marc, Theresa Hiemann, Falk Müller-Riemenschneider, Frank Thalau, Stephanie Roll and Stefan N Willich (2008). 'Association of physical activity with all-cause and cardiovascular mortality: a systematic review and meta-analysis'. In: *European Journal of Preventive Cardiology* 15.3, pp. 239–246.
- NTNU-Discovery (Oct. 2019). *Vil Gi Rullestolen Smarte egenskaper*. URL: <https://ntnudiscovery.no/vil-gi-rullestolen-smarte-egenskaper/>.
- Paluska, Scott A and Thomas L Schwenk (2000). 'Physical activity and mental health'. In: *Sports medicine* 29.3, pp. 167–180.
- Plagenhoef, Stanley, F Gaynor Evans and Thomas Abdelnour (1983). 'Anatomical Data for Analyzing Human Motion'. In: *Research Quarterly for Exercise and Sport* 54.2, pp. 169–178. DOI: 10.1080/02701367.1983.10605290. eprint: <https://doi.org/10.1080/02701367.1983.10605290>. URL: <https://doi.org/10.1080/02701367.1983.10605290>.
- Qualisys (n.d.). *Qualisys Motion Capture System*. URL: https://www.ntnu.edu/documents/221360533/1261844700/Qualysis_0qus_QTM_brief2014.pdf/aab4b882-43ac-4524-818a-9e853df7479e.
- Shampine, Lawrence F and Mark W Reichelt (1997). 'The matlab ode suite'. In: *SIAM journal on scientific computing* 18.1, pp. 1–22.
- Shinbrot, Troy, Celso Grebogi, Jack Wisdom and James A Yorke (1992). 'Chaos in a double pendulum'. In: *American Journal of Physics* 60.6, pp. 491–499.
- Stachowiak, GW, AW Batchelor and LJ Griffiths (1994). 'Friction and wear changes in synovial joints'. In: *Wear* 171.1-2, pp. 135–142.
- Stachowiak, Tomasz and Toshio Okada (2006). 'A numerical analysis of chaos in the double pendulum'. In: *Chaos, Solitons & Fractals* 29.2, pp. 417–422.
- Strumia, Alberto (2018). 'An analytic approach to Van der Pol limit cycle'. In.
- Van De Geer, Sara A (2005). 'Estimation'. In: *Encyclopedia of statistics in behavioral science*, pp. 1041–1045.
- Wall, Michael E, Andreas Rechtsteiner and Luis M Rocha (2003). 'Singular value decomposition and principal component analysis'. In: *A practical approach to microarray data analysis*. Springer, pp. 91–109.
- Widdma (n.d.). *File:Vanderpol-lc.svg*. URL: <https://commons.wikimedia.org/w/index.php?curid=9391038>.

- Wilby, Mary (Oct. 2019). 'Physical Mobility Impairment and Risk for Cardiovascular Disease'.
In: *Health Equity* 3, pp. 527–531. DOI: [10.1089/heap.2019.0065](https://doi.org/10.1089/heap.2019.0065).
- World Health Organization, WHO; Chapal Khasnabis; Johan Borg (2008). *Guidelines On The Provision Of Manual Wheelchairs In Less Resourced Settings*.

Appendix A

Additional Material

A.1 Power series of the Van der Pol limit cycle

A.1.1 Order zero [ε^0]

Consider

$$f_{[0]}(x) = h_0(x) \quad (\text{A.1})$$

which is to be introduced into

$$p_{[0]}(x, \varepsilon) \equiv p(x, 0) \quad (\text{A.2})$$

Using equation (2.7) and (2.8) we get

$$h_{[0]}(x) \frac{dh_{[0]}(x)}{dx} + x = 0 \iff \frac{d}{dx} \left[\frac{h_{[0]}(x)^2 + x^2}{2} \right] = 0 \quad (\text{A.3})$$

the solution to which provides the Cartesian equations

$$h_{[0]}^{(\pm)}(x) = \pm \sqrt{A^2 - x^2} \implies f_{[0]}^{(\pm)}(x) = \pm \sqrt{A^2 - x^2} \quad (\text{A.4})$$

where A is a constant depending on the boundary conditions.

A.1.2 Order one [ε^1]

Consider

$$f_{[1]}(x) = h_{[0]}(x) + h_{[1]}(x)\varepsilon \quad (\text{A.5})$$

where $h_{[0]}(x)$ is given by the result in ???. Then we have to test the functions, related to two branches of the integral curve

$$f_{[1]}^{(\pm)}(x) = \pm \sqrt{A^2 - x^2} + h_{[1]}^{(\pm)}(x)\varepsilon \quad (\text{A.6})$$

where $h_{[1]}^{(\pm)}(x)$ are to be determined from when the Taylor polynomial

$$p_{[1]}(x, \varepsilon) = p_{(x,0)} + \frac{\partial p}{\partial \varepsilon}(x, 0)\varepsilon \quad (\text{A.7})$$

equals zero when non-linear powers of ε are neglected. Calculations lead to the differential equation

$$(A^2 - x^2) \frac{dh_{[1]}^{(\pm)}(x)}{dx} - xh_{[1]}^{(\pm)}(x) = (A^2 - x^2)(1 - x^2) \quad (\text{A.8})$$

to which the solution is given by

$$h_{[1]}^{(\pm)}(x) = \frac{1}{8} \left[\frac{A^2(4 - A^2)}{\sqrt{A^2 - x^2}} \sin^{-1}\left(\frac{x}{A}\right) + (A^2x - 2x^3 + 4x) \right] + \frac{C^{(\pm)}}{\sqrt{A^2 - x^2}}, \quad (\text{A.9})$$

where $C^{(\pm)}$ are integration constants. Using $A^2 = 4$ and $C^{(\pm)} = 0$ the solution becomes

$$f_{[1]}^{(\pm)}(x) = \pm \sqrt{4 - x^2} + \left(x - \frac{x^3}{4} \right) \varepsilon \quad (\text{A.10})$$

A.1.3 Order two [ε^2]

At the second order of approximation we consider

$$f_{[2]}(x) = h_{[0]}(x) + h_{[1]}(x)\varepsilon + h_{[2]}(x)\varepsilon^2, \quad (\text{A.11})$$

where $h_{[0]}(x)$ and $h_{[1]}(x)$ are provided from the equations (A.4) and (A.9), it follows that

$$f_{[2]}^{(\pm)}(x) = \pm \sqrt{A^2 - x^2} + \frac{1}{8} \left[\frac{A^2(4 - A^2)}{\sqrt{A^2 - x^2}} \sin^{-1}\left(\frac{x}{A}\right) + (A^2x - 2x^3 + 4x) + \frac{C^{(\pm)}}{\sqrt{A^2 - x^2}} \right] \varepsilon + h_{[2]}^{(\pm)}(x)\varepsilon^2, \quad (\text{A.12})$$

where $h_{[2]}(x)$ is determined from when the third order Taylor polynomial

$$p_{[2]}(x, \varepsilon) = p(x, 0) + \frac{\partial p}{\partial \varepsilon}(x, 0)\varepsilon + \frac{1}{2} \frac{\partial^2 p}{\partial \varepsilon^2}(x, 0)\varepsilon^2 \quad (\text{A.13})$$

equals zero when cubic powers of ε or higher are neglected. Substitution of equation (A.12) into equation (A.13) leads to

$$\begin{aligned}
& x \sin^{-1}\left(\frac{x}{A}\right)^2 A^8 + \sqrt{A^2 - x^2} \left\{ -2x^2 \sin^{-1}\left(\frac{x}{A}\right) A^6 + \left[4x^4 \sin^{-1}\left(\frac{x}{A}\right) + 64 \frac{dh_2^{(\pm)}(x)}{dx} \right] A^4 + \right. \\
& + \left. \left[(32x^2 - 16x^4) \sin^{-1}\left(\frac{x}{A}\right) - 128x^2 \frac{dh_2^{(\pm)}(x)}{dx} - 64x h_2^{(\pm)}(x) + 16C^{(\pm)} x^2 \right] A^2 + \right. \\
& + \left. 64x^4 \frac{dh_2^{(\pm)}(x)}{dx} + 64x^3 h_2^{(\pm)}(x) - 32C^{(\pm)} x^4 + 64C^{(\pm)} x^2 \right\} + \left[x^3 - 8x \sin^{-1}\left(\frac{x}{A}\right)^2 \right] A^6 + \\
& + \left[16x \sin^{-1}\left(\frac{x}{A}\right)^2 - 16C^{(\pm)} x \sin^{-1}\left(\frac{x}{A}\right) - 5x^5 + 8x^3 \right] A^4 + \left[64C^{(\pm)} x \sin^{-1}\left(\frac{x}{A}\right) + \right. \\
& + \left. 8x^7 - 24x^5 + 16x^3 \right] A^2 - 4x^9 + 16x^7 - 16x^5 + 64 [C^{(\pm)}]^2 x = 0.
\end{aligned} \tag{A.14}$$

which becomes dramatically simplified with the parameter choices

$$|A| = 2, \quad C^{(\pm)} = 0 \tag{A.15}$$

which results in

$$\frac{dh_{[2]}^{(\pm)}(x)}{dx} - \frac{x h_{[2]}^{(\pm)}(x)}{4 - x^2} + \frac{x^3}{16} \sqrt{4 - x^2} = 0 \tag{A.16}$$

which, by integration yields

$$h_{[2]}^{(\pm)}(x) = \pm \frac{x^6 - 6x^4 + 32}{96\sqrt{4 - x^2}}. \tag{A.17}$$

Giving us the second order approximation of the Van der Pol limit cycle as

$$f_{[2]}^{(\pm)}(x) = \pm \sqrt{4 - x^2} + \left(x - \frac{x^3}{4} \right) \epsilon \pm \frac{x^6 - 6x^4 + 32}{96\sqrt{4 - x^2}} \epsilon^2 \tag{A.18}$$

A.1.4 Order three [ϵ^3]

At the second order of approximation we consider

$$f_{[3]}(x) = h_{[0]}(x) + h_{[1]}(x)\epsilon + h_{[2]}(x)\epsilon^2 + h_{[3]}(x)\epsilon^3, \tag{A.19}$$

where $h_{[0]}$, $h_{[1]}$ and $h_{[2]}$ are known from previous calculations. $h_{[3]}$ will be determined from when the third order Taylor polynomial

$$p_{[3]}(x, \epsilon) = p(x, 0) + \frac{\partial p}{\partial \epsilon}(x, 0)\epsilon + \frac{1}{2} \frac{\partial^2 p}{\partial \epsilon^2}(x, 0)\epsilon^2 + \frac{1}{6} \frac{\partial^3 p}{\partial \epsilon^3}(x, 0)\epsilon^3 \tag{A.20}$$

becomes zero where ϵ^4 and higher orders are dropped.

Substitution of of equation (A.19) into equation (A.20) leads to

$$(96x^2 - 384) \frac{dh_{[3]}^{(\pm)}(x)}{dx} + 96xh_{[3]}^{(\pm)}(x) + x^8 - 9x^6 + 24x^4 - 16x^2 = 0, \quad (\text{A.21})$$

which results in

$$h_{[3]}^{(\pm)}(x) = \frac{\sin^{-1}\left(\frac{x}{2}\right)}{48\sqrt{4-x^2}} - \frac{3x^7 - 22x^5 + 34x^3 + 12x}{2304} + \frac{c^{(\pm)}}{\sqrt{4-x^2}}. \quad (\text{A.22})$$

Setting $c^{(\pm)} = 0$ we obtain the the third order approximation of the Van der Pol limit cycle as

$$\begin{aligned} f_{[3]}^{(\pm)} = & \pm \sqrt{4-x^2} + \left(x - \frac{x^3}{4}\right) \epsilon \pm \frac{x^6 - 6x^4 + 32}{96\sqrt{4-x^2}} \epsilon^2 + \\ & + \left(\frac{\sin^{-1}\left(\frac{x}{2}\right)}{48\sqrt{4-x^2}} - \frac{3x^7 - 22x^5 + 34x^3 + 12x}{2304}\right) \epsilon^3 \end{aligned} \quad (\text{A.23})$$

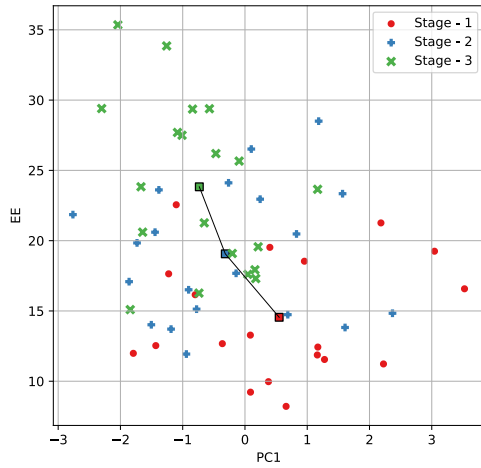
A.2 Atan2

atan2 is calculated as follows

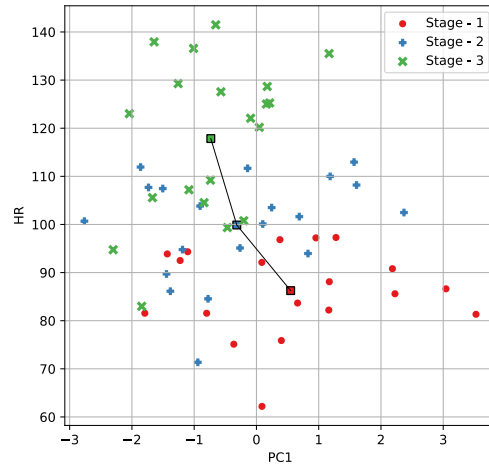
$$\text{atan2}(y, x) = \begin{cases} \arctan\left(\frac{y}{x}\right) & \text{if } x > 0 \\ \arctan\left(\frac{y}{x}\right) + \pi & \text{if } x < 0 \text{ and } y \geq 0 \\ \arctan\left(\frac{y}{x}\right) - \pi & \text{if } x < 0 \text{ and } y < 0 \\ +\frac{\pi}{2} & \text{if } x = 0 \text{ and } y > 0 \\ -\frac{\pi}{2} & \text{if } x = 0 \text{ and } y < 0 \\ \text{undefined} & \text{if } x = 0 \text{ and } y = 0. \end{cases} \quad (\text{A.24})$$

A.3 Plots

A.3.1 Double pendulum estimator correlations with HR and EE

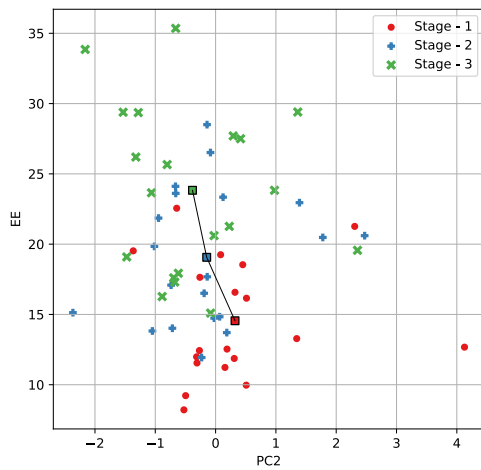


(a) Third order approximations.

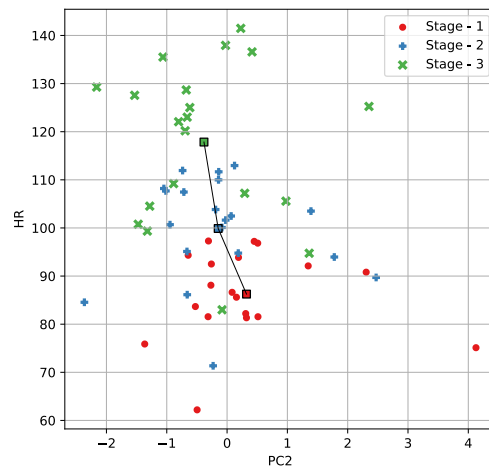


(b) RK4 solutions.

Figure A.1: Phase portraits of the third order approximations and RK4 solutions of the limit cycle.

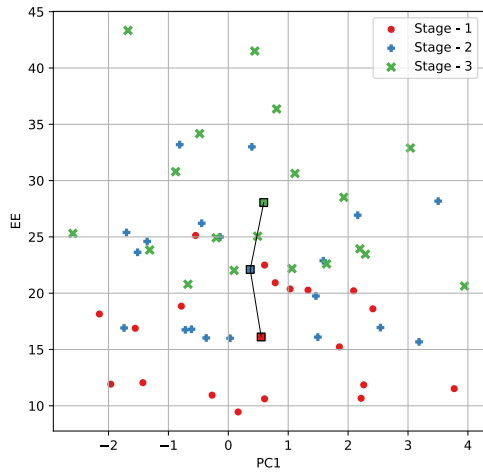


(a) Third order approximations.

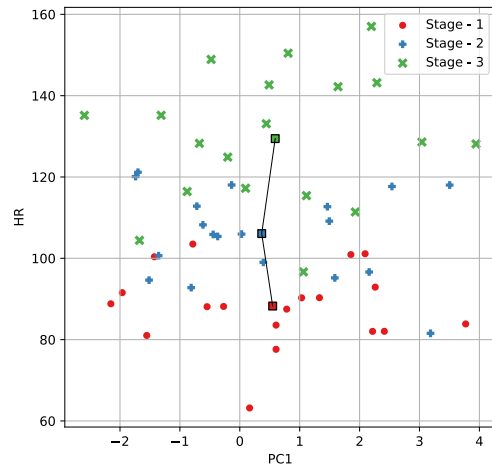


(b) RK4 solutions.

Figure A.2: Phase portraits of the third order approximations and RK4 solutions of the limit cycle.

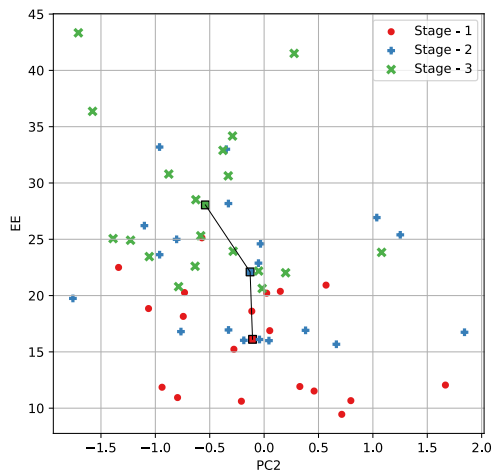


(a) PC1 plotted against EE.

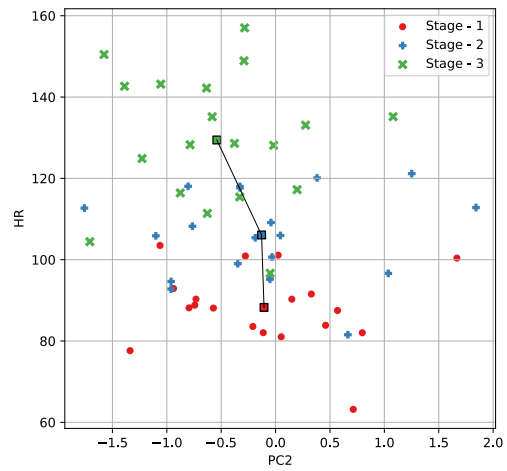


(b) PC1 plotted against HR.

Figure A.3: Scatter plot from the 2.5% incline test day of the first principal component against energy expenditure and heart rate. The center of the clusters from each stage are marked as squares.



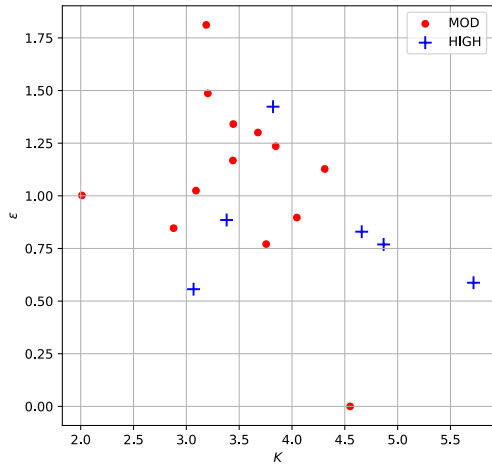
(a) PC2 plotted against EE.



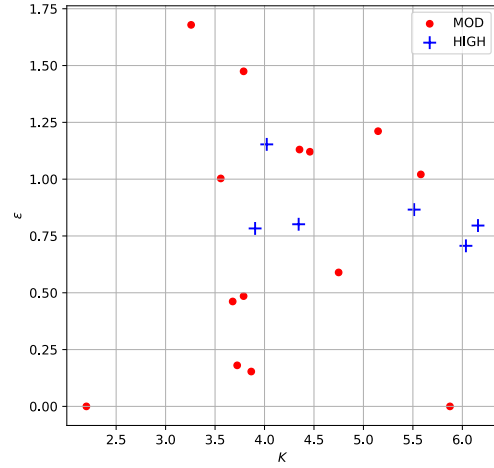
(b) PC2 plotted against HR.

Figure A.4: Scatter plot from the 2.5% incline test day of the second principal component against energy expenditure and heart rate. The center of the clusters from each stage are marked as squares.

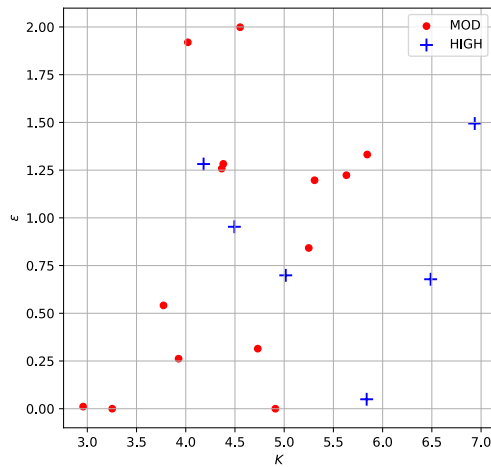
A.3.2 K and ε correlations with IPAQ and Gender



(a) K plotted against ε from interval stage 1.

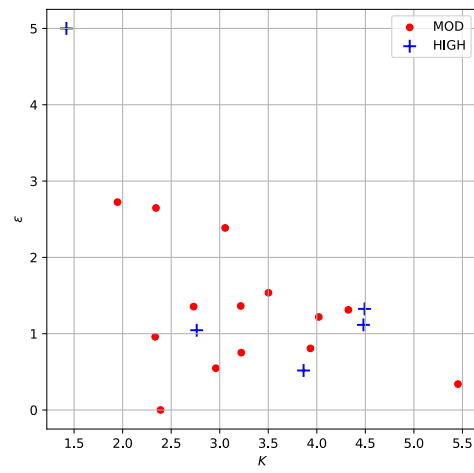
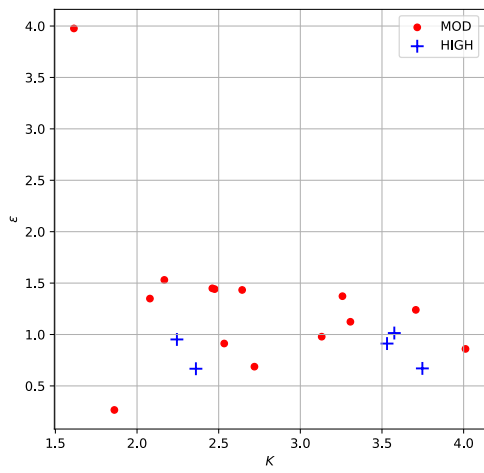


(b) K plotted against ε from interval stage 2.



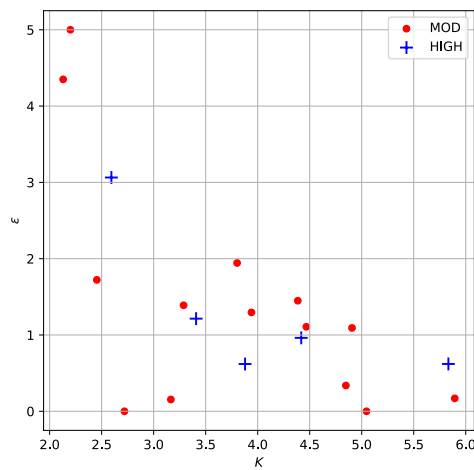
(c) K plotted against ε from interval stage 3.

Figure A.5: K and ε from all participants during the 2.5% test day with IPAQ levels marked as HIGH or MOD (moderate).



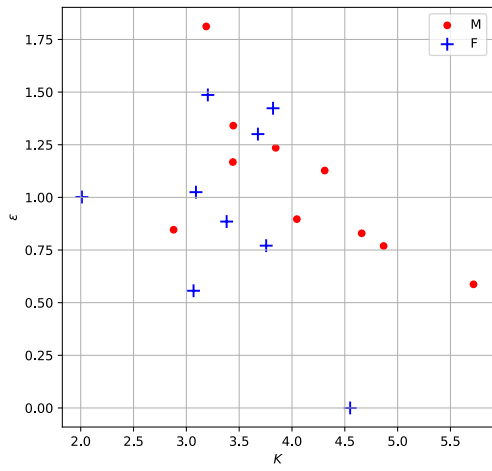
(a) K plotted against ε from interval stage 1.

(b) K plotted against ε from interval stage 2.

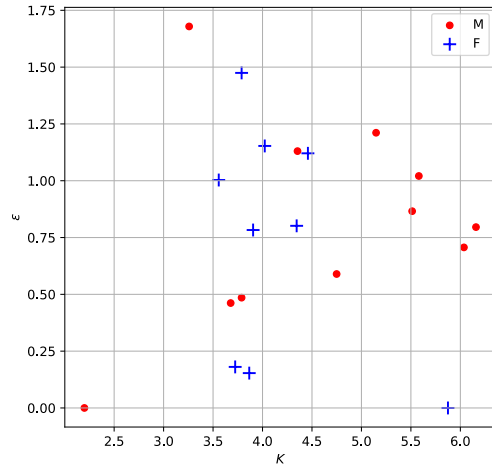


(c) K plotted against ε from interval stage 3.

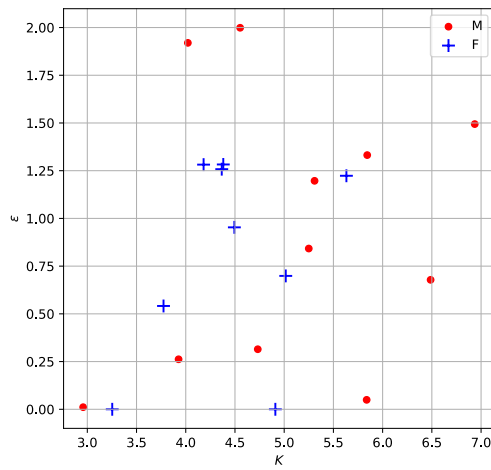
Figure A.6: K and ε from all participants during the 5.0% test day with IPAQ levels marked as HIGH or MOD (moderate).



(a) K plotted against ε from interval stage 1.

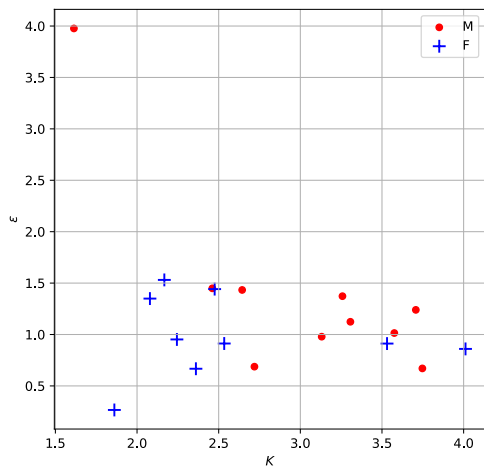


(b) K plotted against ε from interval stage 2.

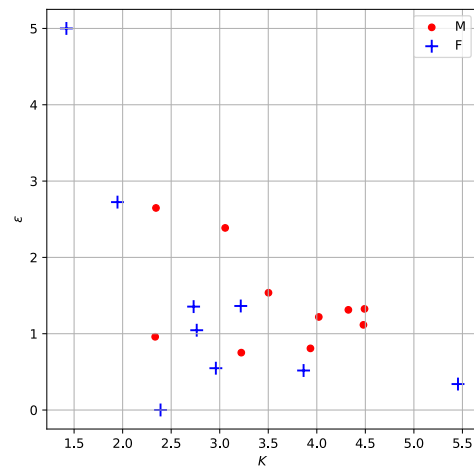


(c) K plotted against ε from interval stage 3.

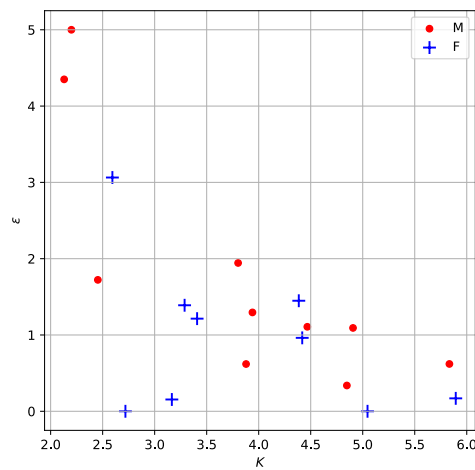
Figure A.7: K and ε from all participants during the 2.5% test day with gender marked as M for male and F for female.



(a) K plotted against ε from interval stage 1.



(b) K plotted against ε from interval stage 2.



(c) K plotted against ε from interval stage 3.

Figure A.8: K and ε from all participants during the 5.0% test day with gender marked as M for male and F for female.

